PARKINSON'S DISEASE

LRRK2 regulates production of reactive oxygen species in cell and animal models of Parkinson's disease

Matthew T. Keeney[1,2,3], Emily M. Rocha[1,2], Eric K. Hoffman[1,2], Kyle Farmer[1,2], Roberto Di Maio[1,2], Julie Weir[1,2], Weston G. Wagner[1,2], Xiaoping Hu[1,2], Courtney L. Clark[1,2], Sandra L. Castro[1,2], Abigail Scheirer[1,2], Marco Fazzari[3], Briana R. De Miranda[1,4], Sean A. Pintchovski[5], William D. Shrader[5], Patrick J. Pagano[3,6], Teresa G. Hastings[1,2], J. Timothy Greenamyre[1,2]*

Oxidative stress has long been implicated in Parkinson's disease (PD) pathogenesis, although the sources and regulation of reactive oxygen species (ROS) production are poorly defined. Pathogenic mutations in the gene encoding leucine-rich repeat kinase 2 (LRRK2) are associated with increased kinase activity and a greater risk of PD. The substrates and downstream consequences of elevated LRRK2 kinase activity are still being elucidated, but overexpression of mutant LRRK2 has been associated with oxidative stress, and antioxidants reportedly mitigate LRRK2 toxicity. Here, using CRISPR-Cas9 gene-edited HEK293 cells, RAW264.7 macrophages, rat primary ventral midbrain cultures, and PD patient–derived lymphoblastoid cells, we found that elevated LRRK2 kinase activity was associated with increased ROS production and lipid peroxidation and that this was blocked by inhibitors of either LRRK2 kinase or NADPH oxidase 2 (NOX2). Oxidative stress induced by the pesticide rotenone was ameliorated by LRRK2 kinase inhibition and was absent in cells devoid of LRRK2. In a rat model of PD induced by rotenone, a LRRK2 kinase inhibitor prevented the lipid peroxidation and NOX2 activation normally seen in nigral dopaminergic neurons in this model. Mechanistically, LRRK2 kinase activity was shown to regulate phosphorylation of serine-345 in the p47^{phox} subunit of NOX2. This, in turn, led to translocation of p47^{phox} from the cytosol to the membrane-associated gp91^{phox} (NOX2) subunit, activation of the NOX2 enzyme complex, and production of ROS. Thus, LRRK2 kinase activity may drive cellular ROS production in PD through the regulation of NOX2 activity.

INTRODUCTION

Parkinson's disease (PD) is a common neurodegenerative disease that results in motor impairment, autonomic dysfunction, and cognitive deficits (*1*). Pathologically it is characterized, in part, by the selective loss of dopaminergic neurons in the substantia nigra (*1*). PD is a multifactorial disease that manifests from the complex interplay between aging, genetics, and the environment, and the mechanisms that lead to neurodegeneration are multifaceted and have yet to be fully elucidated. Longstanding evidence implicates oxidative stress–induced damage as a major contributor to PD pathogenesis (*2*). Specifically, in the substantia nigra of PD postmortem human brain tissue, there are increased amounts of the lipid peroxidation product 4-hydroxynonenal (4-HNE) (*3*) and protein carbonyls (*4*) and diminished amounts of reduced glutathione (*5*), a cellular defense system to combat excessive reactive oxygen species (ROS). Consequences of excessive ROS production and accumulation of lipid peroxidation products include protein damage and dysfunction, organelle failure and, ultimately, cell death. However, the key sources of ROS that lead to oxidative damage in PD have yet to be defined unambiguously.

The two major sources of ROS in most cells are mitochondria and reduced form of nicotinamide adenine dinucleotide phosphate (NADPH) oxidase 2 (NOX2). Mitochondrial dysfunction has been linked to PD, and there are many reports of deficient complex I activity in patients with PD compared with controls (*6*). One consequence of dysfunctional complex I is the formation of cellular ROS (*7*). Increased mitochondrial ROS can lead to activation of NOX2, the major enzymatic source of superoxide anion, in a process called ROS-induced ROS production (*8*). The active NOX2 complex resides at cellular membranes and is made up of the transmembrane proteins NOX2 (previously gp91^{phox}) and p22^{phox} and its associated components: the "organizer" subunit p47^{phox}, p40^{phox}, p67^{phox}, and Rac1 (*9*). Before its activation, p47^{phox}, p40^{phox}, and p67^{phox} exist in a latent, bound trimeric form. Upon p47^{phox} phosphorylation, the trimer forms a complex with Rac1, which then translocates to the membrane, where it interacts with NOX2 and p22^{phox} to generate superoxide anion (*10*, *11*); p47^{phox} phosphorylation and translocation to the membrane are accurate indicators of enzyme assembly and activation. We have recently shown that NOX2 activity is elevated in dopamine neurons and microglia in idiopathic PD (iPD) postmortem human brain tissue (*12*), which suggests that aberrant NOX2 activity may contribute to the oxidative damage observed in PD. Despite this knowledge, the regulation of mitochondrially derived and NOX2-derived ROS, as well as their relative contributions to PD pathogenesis, remains to be defined.

Mutations in the *leucine rich-repeat kinase 2* (*LRRK2*) gene increase the risk of developing PD and are associated with a toxic gain of function, that is, elevated LRRK2 kinase activity (*13*–*16*). Accumulating evidence indicates that nonmutated wild-type (WT) LRRK2 kinase activity is enhanced in iPD (*13*, *17*–*20*); however, the mechanisms by which LRRK2 kinase activity contributes to PD remain unclear. LRRK2 kinase inhibition has been shown to provide neuroprotection in multiple in vivo PD animal models

[1]Pittsburgh Institute for Neurodegenerative Diseases, University of Pittsburgh School of Medicine, Pittsburgh, PA, USA. [2]Department of Neurology, University of Pittsburgh School of Medicine, Pittsburgh, PA, USA. [3]Department of Pharmacology and Chemical Biology, University of Pittsburgh School of Medicine, Pittsburgh, PA, USA. [4]Center for Neurodegeneration and Experimental Therapeutics, Department of Neurology, University of Alabama at Birmingham, Birmingham, AL, USA. [5]Acurex Biosciences, San Carlos, CA, USA. [6]Vascular Medicine Institute, University of Pittsburgh School of Medicine, Pittsburgh, PA, USA.
*Corresponding author. Email: tim.greenamyre@pitt.edu

(*21*–*23*). Overexpression of pathogenic mutant forms of LRRK2 has been associated with enhanced oxidative stress, and antioxidants reportedly mitigate LRRK2-associated toxicity (*24*, *25*). Thus, LRRK2 kinase activity may somehow regulate ROS production and oxidative damage, which, in turn, may contribute to LRRK2-associated toxicity. To date, however, most investigations in this regard have used overexpression systems and mutant LRRK2, so it remains unclear whether endogenous mutant LRRK2 or aberrantly stimulated endogenous WT LRRK2 might regulate cellular ROS.

Here, we provide evidence that LRRK2 kinase activity is a critical regulator of ROS production and oxidative damage in several cellular models of PD. Moreover, we propose a potential mechanism by which endogenous mutant LRRK2 and stimulated WT LRRK2 kinase activity may lead to ROS production and lipid peroxidation.

RESULTS

Endogenous LRRK2 kinase activity regulates ROS production

Overexpression of pathogenic mutant forms of LRRK2 has been associated with increased production of ROS. To determine whether endogenous LRRK2 has an effect on ROS production, we first assessed baseline cytoplasmic superoxide production using dihydroethidium (DHE) in human embryonic kidney 293 (HEK293) cells expressing WT LRRK2. We then compared cytoplasmic superoxide production in CRISPR-Cas9 gene-edited, kinase-activating mutant G2019S LRRK2 (LRRK2$^{GS/GS}$) HEK293 cells and in LRRK2 null (LRRK2$^{-/-}$) HEK293 cells. At baseline, the DHE signal in LRRK2$^{GS/GS}$ cells was elevated in comparison with WT cells [$P < 0.0005$; two-way analysis of variance (ANOVA) with Tukey correction] (Fig. 1, A and B). The selective LRRK2 kinase inhibitor, PF360, blocked ROS production in LRRK2$^{GS/GS}$ cells, suggesting that ROS generation in these cells was dependent on LRRK2 kinase activity ($P < 0.005$; two-way ANOVA with Tukey correction) (Fig. 1, A and B).

Rotenone is a mitochondrial complex I inhibitor that has been used to model aspects of PD in vitro and in vivo (*7*). Binding of rotenone to complex I can cause upstream leak of electrons from the electron transfer chain, and these electrons can react with molecular oxygen to form ROS. Downstream consequences of ROS include oxidative damage to proteins, especially cysteine residues and membrane lipid peroxidation. In WT HEK293 cells, rotenone elicited an increase in ROS (DHE signal) compared with vehicle ($P < 0.0001$; two-way ANOVA with Tukey correction) (Fig. 1, A and B), which was prevented by cotreatment with PF360 (Fig. 1, A and B). Rotenone did not cause ROS production in LRRK2$^{-/-}$ cells ($P = 0.99$; two-way ANOVA with Tukey correction) (Fig. 1, A and B).

Because LRRK2 plays a role in immune cell function, we assessed whether LRRK2 also regulates ROS production in RAW264.7 cells, a mouse macrophage cell line. As a prerequisite, we first demonstrated that rotenone treatment of the macrophages increased the kinase activity of the endogenous LRRK2 contained in these cells. Using a proximity ligation (PL) assay that detects phosphorylation status of the autophosphorylation site pSer^{1292} (PL pSer^{1292}–LRRK2), we showed that rotenone increased endogenous WT LRRK2 kinase activity in RAW264.7 macrophages ($P < 0.0001$; two-way ANOVA with Tukey correction) (fig. S1). Congruent results were obtained using the orthogonal approach of Western blotting of the phosphorylation state of the LRRK2 substrate, Rab10. Rotenone treatment led to an increase in pThr^{73}-Rab10 signal compared with vehicle-treated RAW264.7 cells ($P < 0.005$ one-way ANOVA with Tukey correction) (fig. S1). Treatment with PF360 prevented the rotenone-induced increases in both the PL pSer^{1292}–LRRK2 and pThr^{73}-Rab10 signals (fig. S1). Having demonstrated that rotenone activates WT LRRK2 kinase in RAW264.7 macrophages, we next found that rotenone increased the macrophage DHE signal relative to vehicle ($P < 0.0005$; two-way ANOVA with Tukey correction), an effect that was prevented by PF360 ($P < 0.0001$; two-way ANOVA with Tukey correction) (Fig. 1, A and C). Rotenone did not increase ROS in LRRK2$^{-/-}$ RAW264.7 macrophages ($P = 0.8622$; two-way ANOVA with Tukey correction) (Fig. 1, A and C), consistent with our results in LRRK2$^{-/-}$ HEK293 cells. We also assessed whether rotenone induced DHE signals in cultured rat midbrain dopaminergic [tyrosine hydroxylase positive (TH^{+})] and nondopaminergic (TH^{-}) neurons. Compared with vehicle, rotenone treatment led to an increase in DHE signal preferentially in dopaminergic neurons ($P < 0.001$; two-way ANOVA with Tukey correction) (Fig. 1, D and E). The rotenone-induced DHE signal was prevented in the presence of PF360 ($P < 0.005$; two-way ANOVA with Tukey correction) (Fig. 1, D and E).

We next investigated whether LRRK2 kinase activity–induced ROS production was relevant in patient-derived lymphoblastoid cell lines. Relative to healthy control cells, baseline DHE signal was elevated in lymphoblastoid cell lines derived from patients with iPD and patients harboring a LRRK2 G2019S mutation ($P < 0.001$ for both iPD and G2019S cell lines compared with healthy controls; two-way ANOVA with Tukey correction) (Fig. 1, F and G). The elevated DHE signal in lymphoblastoid cell lines from patients with iPD and G2019S mutation carriers was reduced to healthy control values by treatment with either PF360 or a structurally dissimilar LRRK2 kinase inhibitor, MLi2 ($P < 0.001$ for both inhibitors compared with vehicle in iPD and G2019S; two-way ANOVA with Tukey correction) (Fig. 1, F and G).

As a final demonstration that rotenone-induced ROS production requires LRRK2 kinase activity, WT LRRK2 was overexpressed by transient transfection in LRRK2$^{-/-}$ HEK293 cells. Under these conditions, rotenone-induced DHE signal was only observed in those cells that expressed LRRK2 and not in untransfected cells in the same microscopic field that did not express LRRK2 ($P < 0.0005$; two-way ANOVA with Tukey correction) (Fig. 2, A and B). Moreover, treatment of transfected cells with PF360 blocked the "rescued" rotenone-induced ROS response associated with LRRK2 expression (Fig. 2C). Thus, multiple genetic and pharmacological approaches indicate that LRRK2 kinase activity is required for both rotenone-induced and PD-associated ROS production.

Sustained ROS production and oxidative damage can lead to the accumulation of the lipid peroxidation product 4-HNE. To assess 4-HNE, we used 4-HNE immunofluorescence in cells and tissue sections. Control experiments confirmed that the 4-HNE immunofluorescent signal was linearly proportional to the concentration of exogenous 4-HNE added to the cell cultures ($R^2 = 0.89$) (fig. S2). Consistent with an increase in ROS production at baseline in LRRK2$^{GS/GS}$ HEK293 cells, we observed an accumulation of 4-HNE in LRRK2$^{GS/GS}$ compared with WT HEK293 cells ($P < 0.05$; two-way ANOVA with Tukey correction) (Fig. 3, A and B), which was prevented by PF360 ($P < 0.05$; two-way ANOVA with Tukey correction) (Fig. 3, A and B). Treatment with rotenone caused an increase in 4-HNE in WT HEK293 cells ($P < 0.05$ compared with vehicle; two-way ANOVA with Tukey correction) and RAW264.7 macrophages

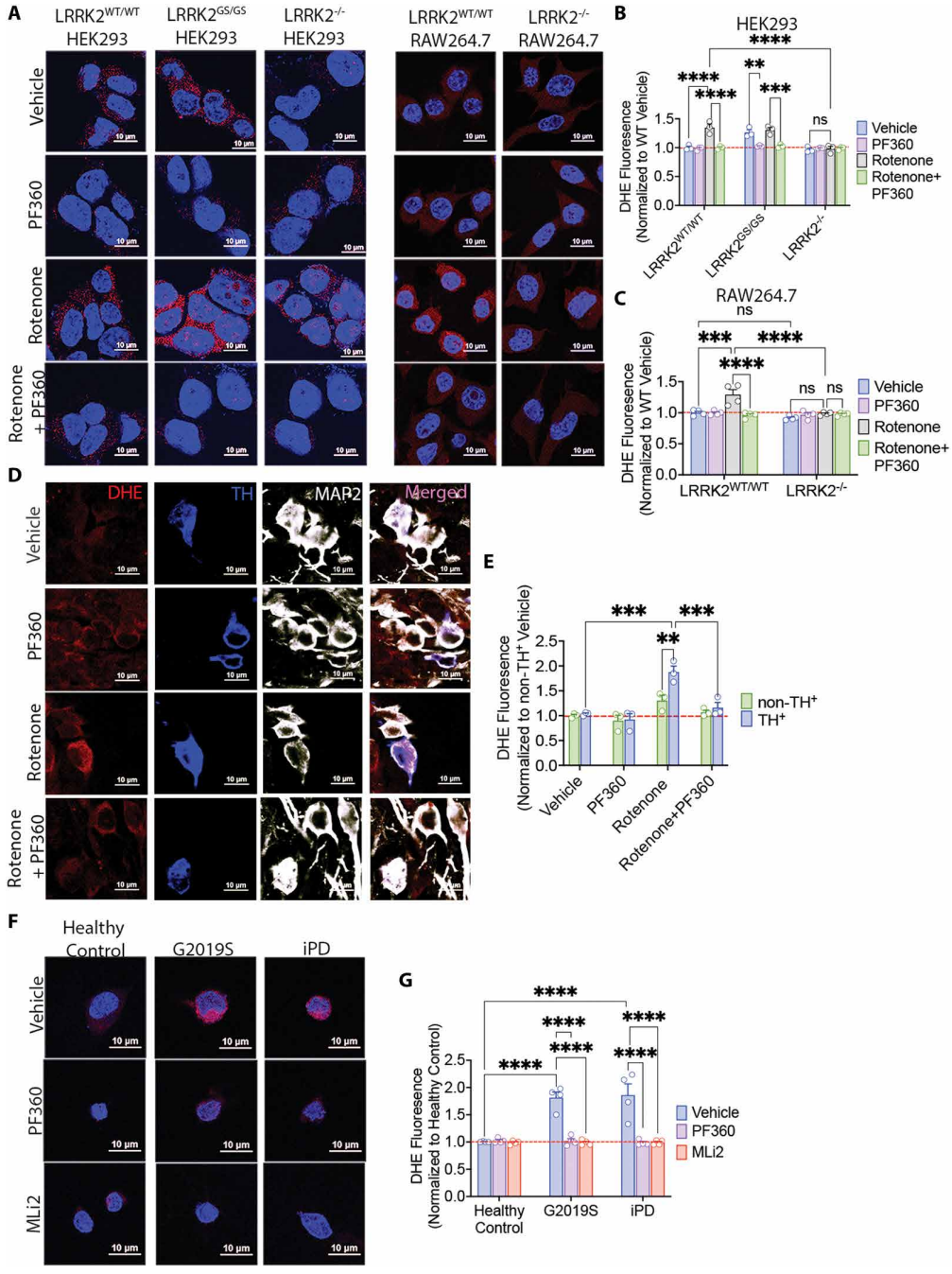

Fig. 1. LRRK2 kinase activity drives ROS production. (**A**) ROS production was assessed by DHE fluorescence (red). LRRK2$^{GS/GS}$-mutant HEK293 cells had an elevated baseline cytosolic DHE signal compared with LRRK2$^{WT/WT}$ cells, which was prevented by treatment with the LRRK2 inhibitor PF360 (1 μM). In WT HEK293 cells or RAW264.7 macrophages, sublethal rotenone (50 nM) treatment increased the DHE signal compared with vehicle. This result was not observed in cells cotreated with PF360 or in LRRK2$^{-/-}$ cells. (**B**) Quantification of normalized DHE signal. Each symbol represents the normalized average DHE signal measured from 100 to 150 cells per treatment group per experiment. $n = 3$ independent experiments. Statistical testing by two-way ANOVA with post hoc Tukey correction; $^{**}P < 0.005$, $^{***}P < 0.0005$, and $^{****}P < 0.0001$; ns, not significant. (**C**) Quantification of normalized DHE signal from WT RAW264.7 cells. DHE measurements are from 100 to 150 cells per treatment group per experiment. $n = 3$ independent experiments. Two-way ANOVA with post hoc Tukey correction; $^{***}P < 0.0005$ and $^{****}P < 0.0001$; ns, not significant. (**D**) Shown is DHE fluorescence (red) in tyrosine hydroxylase (TH; blue) and MAP2 (gray) neurons in rat ventral midbrain primary cultures. Rotenone increased the DHE signal in TH$^+$ neurons, and this was prevented by PF360 treatment. (**E**) Quantification of normalized DHE in TH$^+$/MAP2$^+$ and non-TH$^+$/MAP2$^+$ neurons. DHE signals were normalized to non-TH$^+$ neurons treated with vehicle. Symbols represent normalized average DHE signals measured from 20 to 100 neurons per treatment group per culture. $n = 3$ independent cultures. Statistical testing by two-way ANOVA with post hoc Tukey correction; $^{**}P < 0.05$ and $^{***}P < 0.005$. (**F**) DHE signals in lymphoblastoid cell lines derived from healthy controls, G2019S mutation carriers, and patients with iPD. The increased DHE signals in G2019S and iPD lymphoblastoid cell lines were reduced to healthy control values by both PF360 and MLi2 LRRK2 inhibitors. (**G**) Quantification of normalized DHE signals. Each symbol represents an individual donor cell line. DHE signals were taken from 90 to 120 cells per line; four donor lines per group. Statistical testing by two-way ANOVA with post hoc Tukey correction; $^{****}P < 0.0001$.

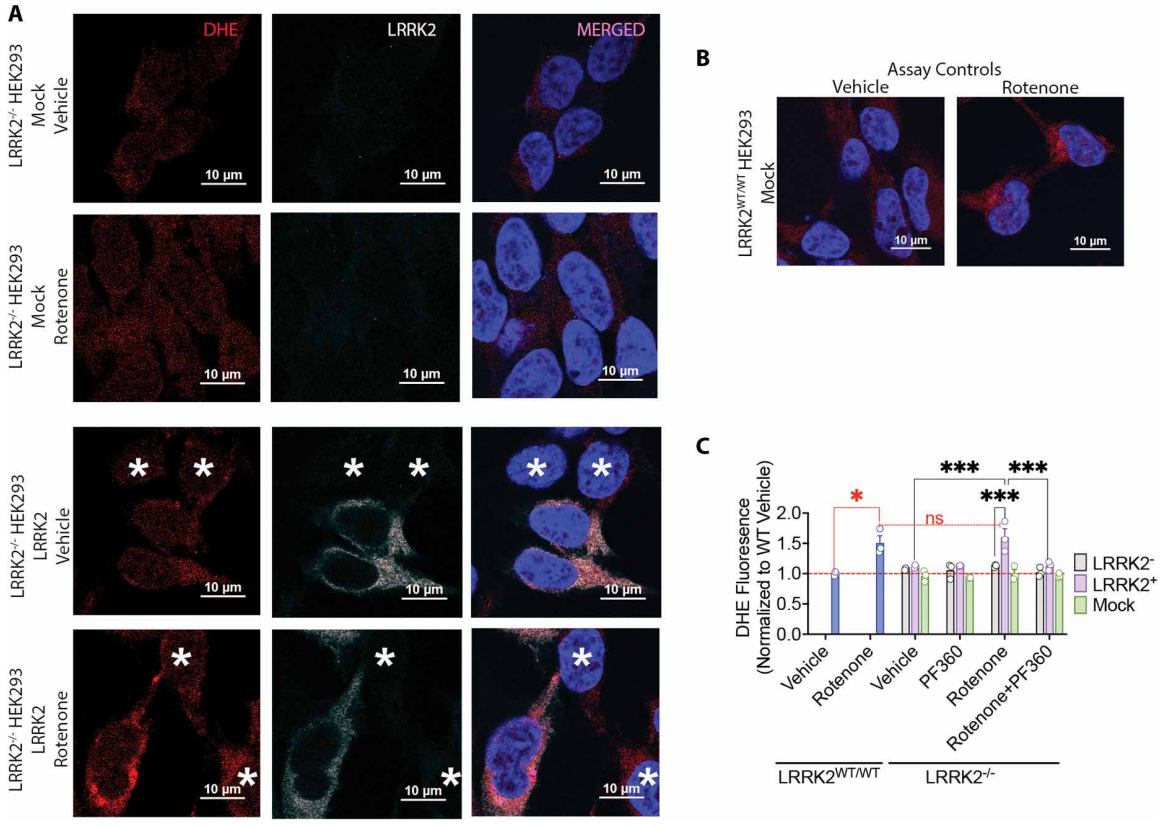

Fig. 2. LRRK2 expression restores rotenone-induced ROS production in LRRK2$^{-/-}$ cells. (**A**) ROS production was assessed by DHE fluorescence (red) in LRRK2$^{-/-}$ HEK293 cells that were mock transfected and treated with vehicle or rotenone (top two rows). ROS production was assessed by DHE fluorescence (red) in LRRK2$^{-/-}$ HEK293 cells transfected with WT LRRK2 and treated with vehicle or rotenone (bottom two rows). Note that in the LRRK2$^{-/-}$ mock-transfected cells, rotenone did not elicit a DHE signal. In contrast, in the LRRK2$^{-/-}$ cells transfected with WT LRRK2, there was a rotenone-induced DHE signal that was absent in adjacent untransfected cells that did not express LRRK2 (asterisks). (**B**) Rotenone elicited an increase in DHE signal in LRRK2$^{WT/WT}$ HEK293 cells compared with vehicle. (**C**) Quantification of normalized DHE signals. Note that blue bars represent WT HEK293 cells, and other bars represent LRRK2$^{-/-}$ cells that were either mock transfected (green) or were transfected with WT LRRK2 and were either LRRK2^{+} (purple) or LRRK2^{-} (gray). Only cells expressing WT LRRK2 had a DHE response to rotenone; PF360 blocked the rotenone response in LRRK2-expressing cells. Each symbol represents the normalized average DHE signal measured from 100 to 150 cells per treatment group per experiment. $n = 3$ independent experiments. Statistical testing by two-way ANOVA with post hoc Tukey correction; ***$P < 0.0005$; ns, not significant.

($P < 0.0001$ compared with vehicle; two-way ANOVA with Tukey correction), which was prevented with PF360; however, rotenone failed to further increase 4-HNE in LRRK2$^{GS/GS}$ cells. Consistent with our previous ROS data, rotenone did not cause an increase in 4-HNE in LRRK2$^{-/-}$ HEK293 cells ($P = 0.99$ compared to vehicle; two-way ANOVA with Tukey correction) or in LRRK2$^{-/-}$ RAW264.7 macrophages ($P = 0.99$ compared to vehicle; two-way ANOVA with Tukey correction) (Fig. 3, A to C).

We next assessed whether rotenone induced 4-HNE accumulation in rat midbrain dopaminergic (TH^{+}) and nondopaminergic (TH^{-}) neurons. Congruent with our DHE results, rotenone treatment led to an accumulation of 4-HNE only in dopaminergic neurons, not in nondopaminergic neurons, ($P < 0.0001$; two-way ANOVA with Tukey correction) (Fig. 3, D and E), and cotreatment with PF360 blocked the rotenone-induced 4-HNE accumulation ($P < 0.0001$; two-way ANOVA with Tukey correction) (Fig. 3, D and E). Similar to our DHE findings in the patient-derived lymphoblastoid cell lines (Fig. 1, F and G), there was elevated 4-HNE in lymphoblastoid cell lines derived from G2019S mutation carriers and patients with iPD compared with those of healthy controls ($P < 0.0001$; two-way ANOVA with Tukey correction) (Fig. 3, F and G). LRRK2 inhibition by either PF360 or MLi2 effectively reduced the elevated 4-HNE signal in lymphoblastoid cell lines derived from G2019S mutation carriers and patients with iPD to healthy control values ($P < 0.0001$; two-way ANOVA with Tukey correction) (Fig. 3, F and G). Together, these results indicate that endogenous mutant and aberrant WT LRRK2 kinase activity regulates ROS production and lipid peroxidation in vitro in HEK293 cells, RAW264.7 macrophages, rat nigral dopaminergic neurons, and patient-derived lymphoblastoid cell lines.

LRRK2 inhibition prevents lipid peroxidation and neurodegeneration in a rat model of PD

Next, to evaluate the in vivo relevance of these findings, we used a rat model of PD. As described previously (*23*), middle-aged rats were treated with rotenone, with or without concomitant cotreatment with the brain-permeant LRRK2 kinase inhibitor PF360 (5 mg/kg BID) for 7 to 10 days until they reached a behavioral end point, at which time they were euthanized for analysis. In rotenone-treated animals, there was a marked increase in LRRK2 kinase activity (PL pS1292–LRRK2

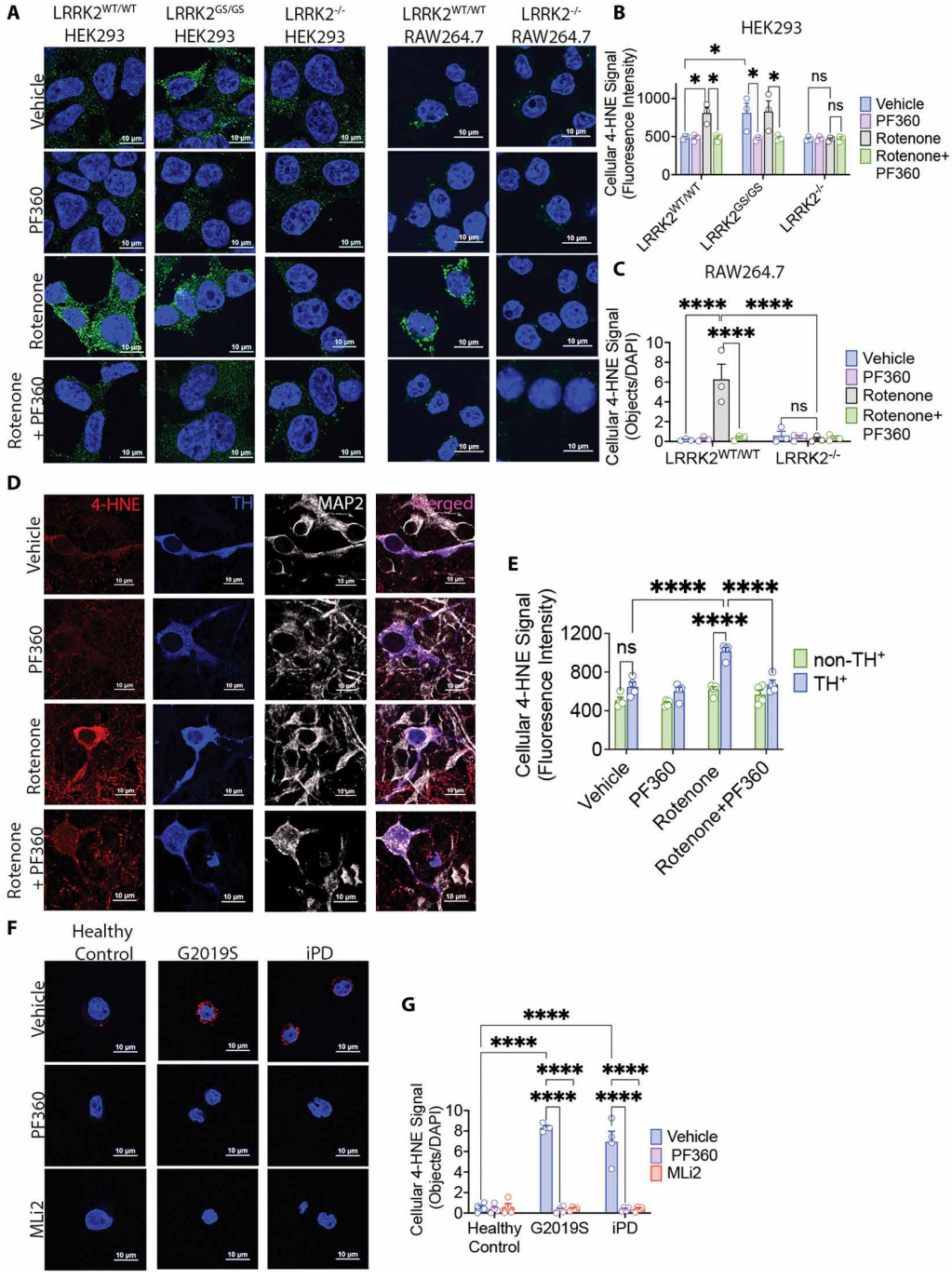

Fig. 3. LRRK2 kinase activity-dependent lipid peroxidation. (**A**) Immunofluorescence staining for 4-HNE (green), a marker of lipid peroxidation, in HEK293 cells and RAW264.7 macrophages. Under basal conditions, there was elevated 4-HNE signal in LRRK2$^{GS/GS}$ HEK293 cells that was reduced by PF360 treatment. In WT HEK293 cells and RAW264.7 macrophages, rotenone increased 4-HNE signals. PF360 or genetic knockout of LRRK2 prevented the rotenone-induced increase in 4-HNE signals. (**B**) Quantification of 4-HNE signals in HEK293 cells. Symbols represent mean signal taken from 100 to 150 cells per treatment group per experiment. $n = 3$ independent experiments. Statistical testing by two-way ANOVA with post hoc Tukey correction; *$P < 0.05$; ns, not significant. (**C**) Quantification of 4-HNE in RAW264.7 macrophages. Each symbol represents mean values obtained from 100 to 150 cells per treatment group per experiment. $n = 3$ independent experiments. ****$P < 0.0001$; ns, not significant. (**D**) Immunofluorescent staining for 4-HNE (red) in TH$^+$ (blue) and MAP2$^+$ (gray) neurons in primary cultures of rat ventral midbrain. Rotenone increased the 4-HNE signal only in TH$^+$ neurons, and this was prevented by PF360 treatment. (**E**) Quantification of 4-HNE in TH$^+$/MAP2$^+$ and non-TH$^+$/MAP2$^+$ neurons. Symbols represent mean 4-HNE signals from 20 to 100 neurons per treatment group per culture. $n = 4$ independent cultures. ****$P < 0.0001$. (**F**) 4-HNE signals in lymphoblastoid cell lines derived from healthy controls, G2019S mutation carriers, and patients with iPD. The increased 4-HNE signals in G2019S and iPD lymphoblastoid cell lines were reduced to healthy control values by either PF360 or Mli2. (**G**) Quantification of 4-HNE. Each symbol represents an individual donor cell line. 4-HNE signals were taken from 90 to 120 cells per line; four donor lines per group. Statistical testing by two-way ANOVA with post hoc Tukey correction; ****$P < 0.0001$.

signal) in substantia nigra dopaminergic neurons ($P < 0.0001$; one-way ANOVA with Tukey correction) (fig. S3). Concomitant treatment with PF360 blocked the increase in LRRK2 kinase activity (fig. S3). To assess rotenone-induced oxidative damage, we evaluated the accumulation of 4-HNE. Rotenone treatment increased 4-HNE in nigral dopaminergic neurons compared with nigral dopaminergic neurons from vehicle-treated rats ($P < 0.005$; one-way ANOVA with Tukey correction) (Fig. 4, A and B). PF360 cotreatment prevented rotenone-induced 4-HNE accumulation ($P < 0.005$; one-way ANOVA with Tukey correction) (Fig. 4, A and B). Histopathological analysis revealed that rotenone alone caused a significant loss in TH^+ and Nissl-positive nigral dopaminergic neurons ($P < 0.005$; one-way ANOVA with Tukey correction), and cotreatment with PF360 prevented this loss of dopaminergic neurons (Fig. 4, C and D). These results are consistent with the in vitro results, suggesting that oxidative damage (lipid peroxidation) may be regulated by LRRK2 kinase activity.

NADPH oxidase 2 is the major source of ROS regulated by LRRK2 kinase activity

To investigate how LRRK2 activity leads to ROS production, we first examined mitochondrial ROS production using the mitochondrial superoxide indicator mtSOX–deep red. At baseline, we observed elevated mtSOX signal in $LRRK2^{GS/GS}$ compared with WT HEK293 cells ($P < 0.0001$; two-way ANOVA with Tukey correction) (Fig. 5, A and B, and fig. S4, A and B), which was reduced by treatment with PF360 ($P < 0.0001$; two-way ANOVA with Tukey correction) (Fig. 5, A and B) or the mitochondrial ROS scavenger mitoTEMPO ($P < 0.005$; two-way ANOVA with Tukey correction) (fig. S4, A and B). The mtSOX signal was reduced by mitoTEMPO, indicating that the mtSOX signal was specific for mitochondria. The mitochondrial ROS signal was blocked by PF360, confirming that it was dependent on LRRK2 kinase activity. To ensure this finding was a result of increased LRRK2 kinase activity and not an undefined G2019S mutation effect, we generated CRISPR-Cas9 gene-edited HEK293 cells that harbored another LRRK2 kinase–activating mutation, R1441G ($LRRK2^{RG/RG}$). Congruent with our earlier findings, compared with WT HEK293 cells, $LRRK2^{RG/RG}$ HEK293 cells had an elevated basal mtSOX signal, like the $LRRK2^{GS/GS}$ cells ($P < 0.001$; two-way ANOVA with Tukey correction) (fig. S4, C and D). Treatment with the LRRK2 inhibitor MLi2 reduced the mtSOX signal in both $LRRK2^{RG/RG}$ cells ($P < 0.01$; two-way ANOVA with Tukey correction) and $LRRK2^{GS/GS}$ cells ($P < 0.0005$; two-way ANOVA with Tukey correction) down to WT values (fig. S4, C and D).

In addition to mitochondria, NOX2 is a major source of cellular ROS production, and we have previously reported that there is enhanced NOX2 activity in nigral dopaminergic neurons and microglia derived from patients with iPD (*12*). Moreover, rotenone-induced

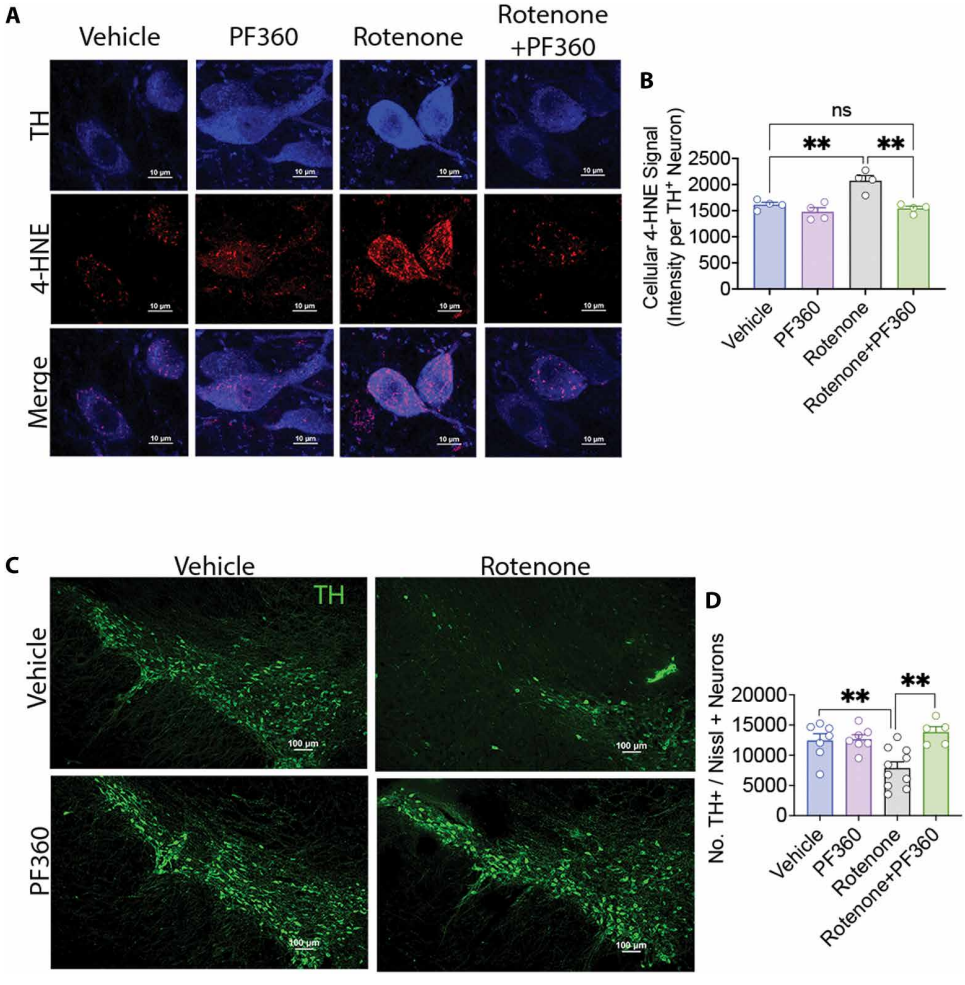

Fig. 4. LRRK2 kinase inhibition prevents lipid peroxidation and neurodegeneration in a rat model of PD. (**A**) Immunofluorescence staining for 4-HNE (red) in TH^+ dopaminergic neurons (blue) in the substantia nigra of rats treated with rotenone in the presence or absence of PF360. Rotenone treatment caused an increase in 4-HNE in TH^+ dopaminergic neurons, and cotreatment with PF360 prevented the rotenone-induced 4-HNE accumulation. (**B**) Quantification of 4-HNE fluorescence intensity per TH^+ neuron. Each symbol represents mean 4-HNE signal per animal. Statistical testing by two-way ANOVA with post hoc Tukey correction. $^{**}P < 0.005$. (**C**) Representative images of TH staining (green) of substantia nigra dopaminergic neurons of rats treated with rotenone with or without cotreatment with PF360. (**D**) Stereological counts of nigral dopaminergic neurons. Each symbol represents an individual animal. Statistical testing by two-way ANOVA with post hoc Tukey correction. $^{**}P < 0.005$.

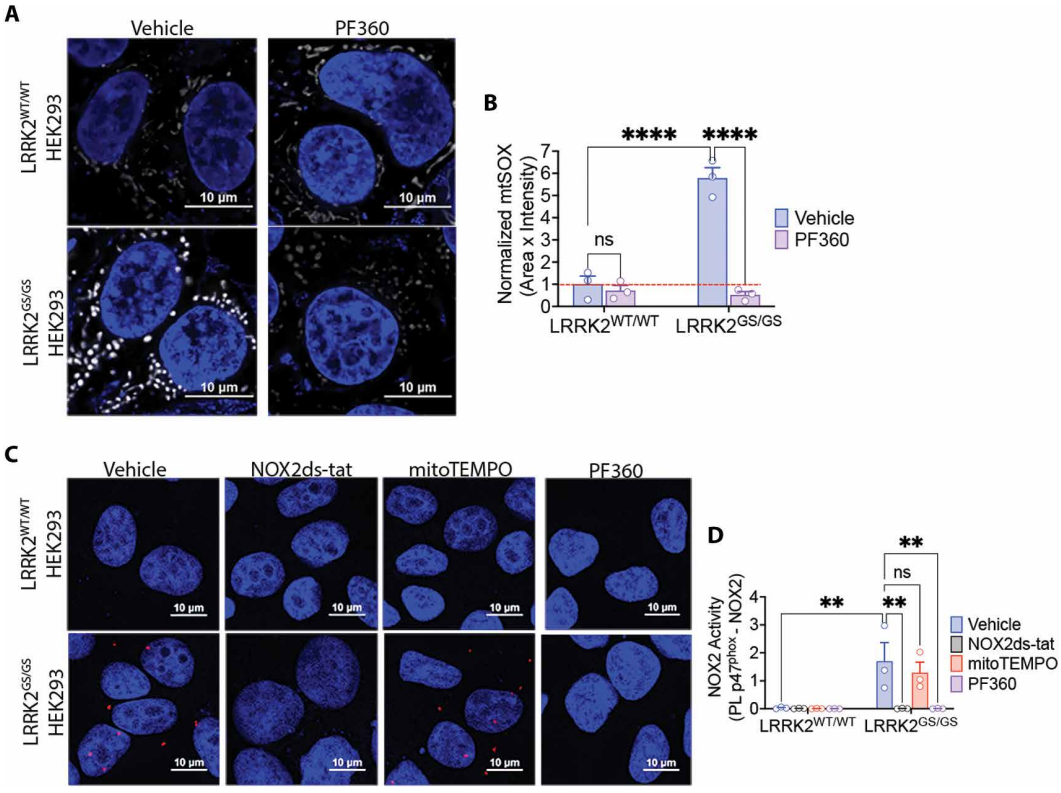

Fig. 5. LRRK2 kinase activity promotes mitochondrial ROS production and NOX2 activation. (**A**) Mitochondrial ROS production was measured using mtSOX in LRRK2$^{WT/WT}$ and LRRK2$^{GS/GS}$ HEK293 cells. LRRK2$^{GS/GS}$ HEK293 cells had a stronger mtSOX signal compared with LRRK2$^{WT/WT}$ under basal conditions. Treatment with PF360 decreased the elevated mtSOX signal in LRRK2$^{GS/GS}$ cells. (**B**) Quantification of normalized mtSOX signals. Each symbol represents the normalized mtSOX signal from 100 to 150 cells per treatment group for each independent experiment. $n = 3$ independent experiments. Statistical testing by two-way ANOVA with post hoc Tukey correction. ****$P < 0.0001$; ns, not significant. (**C**) NOX2 activity assessed by the PL assay, PL p47^{phox}–NOX2 (red dots), in LRRK2$^{WT/WT}$ and LRRK2$^{GS/GS}$ HEK293 cells. Compared with LRRK2$^{WT/WT}$ cells, there was an increased PL p47^{phox}–NOX2 signal in LRRK2$^{GS/GS}$ cells. Treatment with the NOX2 inhibitor NOX2ds-tat (10 µM) or PF360 (1 µM) decreased PL p47^{phox}–NOX2 signal in LRRK2$^{GS/GS}$ cells. The mitochondrial ROS scavenger mitoTEMPO (25 nM) did not prevent the elevated PL p47^{phox}–NOX2 signal in LRRK2$^{GS/GS}$ cells. (**D**) Quantification of PL p47^{phox}–NOX2. Each symbol represents the average number of PL p47^{phox}–NOX2 red dots per cell (as defined by DAPI staining, blue) obtained from 100 to 150 cells per treatment group per independent experiment. $n = 3$ independent experiments. Statistical testing by two-way ANOVA with post hoc Tukey correction. **$P < 0.01$; ns, not significant.

ROS production is markedly amplified by the activation of NOX2. Here, using a validated PL assay for NOX2 activity (PL p47^{phox}–NOX2), we detected an increase in NOX2 activity in LRRK2$^{GS/GS}$ HEK293 cells compared with WT HEK293 cells ($P < 0.01$; two-way ANOVA with Tukey correction) (Fig. 5, C and D). The peptide NOX2 assembly inhibitor (*26*, *27*), NOX2ds-tat, blocked the PL p47^{phox}–NOX2 signal, confirming specificity and source of the PL signal in the LRRK2$^{GS/GS}$ HEK293 cells ($P < 0.01$; two-way ANOVA with Tukey correction) (Fig. 5, C and D). Increased mitochondrial ROS can lead to NOX2 activation in a process called ROS-induced ROS production. Unexpectedly, however, mitoTEMPO did not diminish the NOX2 PL signal in LRRK2$^{GS/GS}$ HEK293 cells ($P = 0.95$; two-way ANOVA with Tukey correction), whereas PF360 completely suppressed the NOX2 signal ($P < 0.01$; two-way ANOVA with Tukey correction) (Fig. 5, C and D). Control experiments showed that neither NOX2ds-tat nor mitoTEMPO inhibited G2019S-driven LRRK2 kinase activity (fig. S5). Together, these results indicate that LRRK2 kinase activity may regulate NOX2 activation.

To determine whether mitochondria or NOX2 was the predominant source of ROS in the presence of kinase-active LRRK2, we sought to define the interventions that would block the baseline LRRK2$^{GS/GS}$-dependent DHE signal. LRRK2$^{GS/GS}$ HEK293 cells were treated with NOX2ds-tat, mitoTEMPO, a scrambled version of NOX2ds-tat (Scrm-NOX2ds-tat), or the thiol antioxidant *N*-acetylcysteine. Whereas neither the scrambled peptide nor mitoTEMPO had any effect, NOX2ds-tat reduced the DHE signal in LRRK2$^{GS/GS}$ HEK293 cells ($P < 0.0001$ compared to LRRK2$^{GS/GS}$ vehicle; two-way ANOVA with Tukey correction) (Fig. 6, A to D), suggesting that the G2019S mutation–driven increase in DHE signal was because of NOX2 activation. *N*-acetylcysteine also dampened the DHE signal in LRRK2$^{GS/GS}$ HEK293 cells, presumably by quenching the NOX2-generated ROS ($P < 0.0001$; two-way ANOVA with Tukey correction) (Fig. 6, A to D). To confirm these findings using an alternate approach, we measured a downstream consequence of excessive ROS production, 4-HNE accumulation, under similar experimental conditions and found that only NOX2ds-tat reduced the baseline 4-HNE accumulation in LRRK2$^{GS/GS}$ HEK293 cells ($P < 0.0001$; two-way ANOVA with Tukey correction) (fig. S6).

Next, we sought to explore whether NOX2 was also the predominant ROS source in RAW264.7 macrophages. First, we examined rotenone-induced NOX2 activity via PL p47^{phox}–NOX2. Rotenone treatment increased the NOX2 signal in WT RAW264.7 macrophages ($P < 0.0001$; two-way ANOVA with Tukey correction) (fig. S7, A and

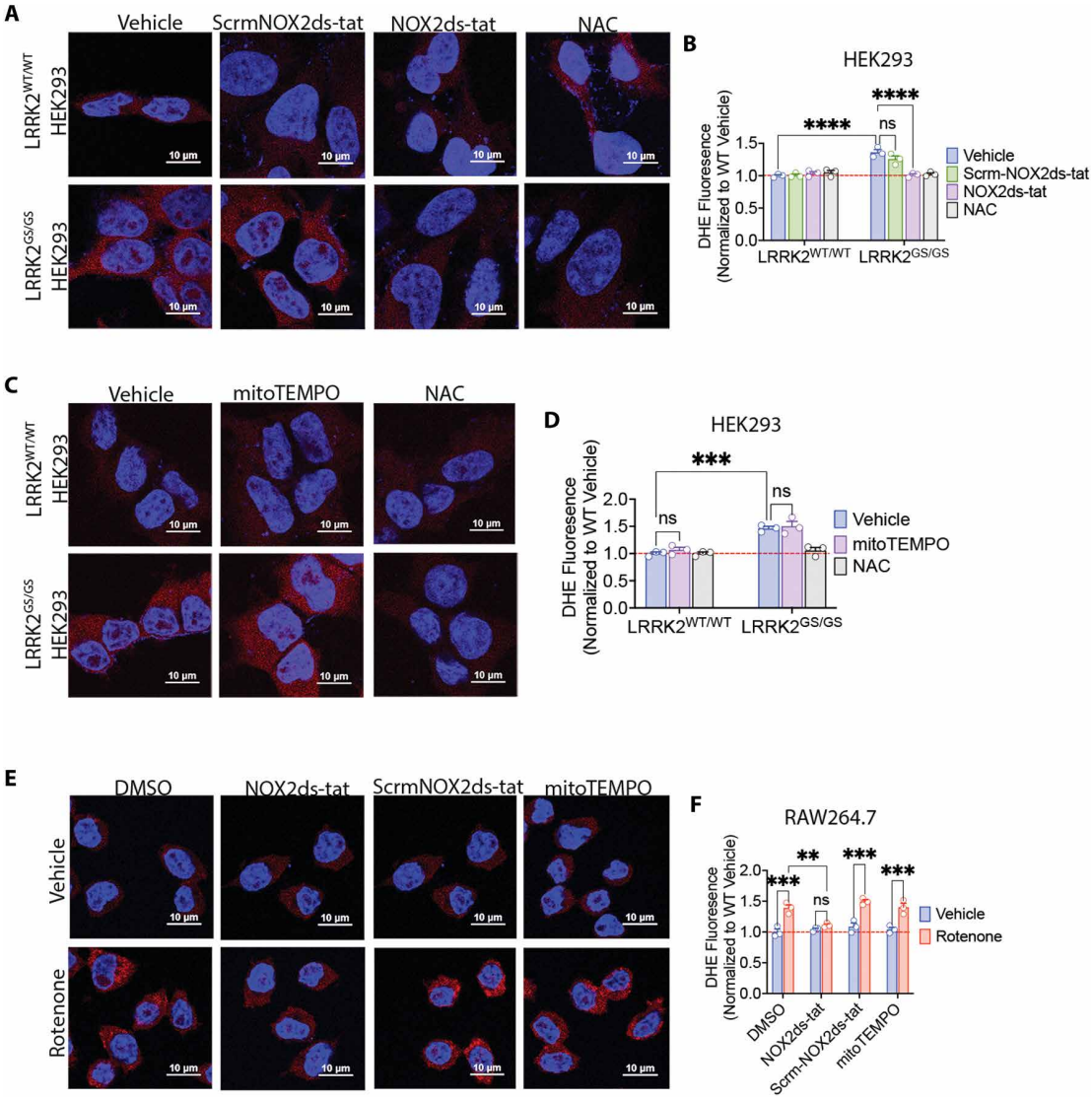

Fig. 6. NOX2 activity is the major source of ROS in the presence of kinase-active LRRK2. (**A**) Cellular ROS production was measured by DHE fluorescence in LRRK2$^{WT/WT}$ and LRRK2$^{GS/GS}$ HEK293 cells. Basal DHE signal was elevated in LRRK2$^{GS/GS}$ compared with LRRK2$^{WT/WT}$ HEK293 cells. Treatment of LRRK2$^{GS/GS}$ cells with NOX2ds-tat or 250 μM *N*-acetylcysteine (NAC) reduced the DHE signal to WT values; however, treatment with a scrambled variant of NOX2ds-tat, Scrm-NOX2ds-tat, had no effect. (**B**) Quantification of normalized cellular DHE signal. DHE signal was measured in 100 to 150 cells per treatment group in each experiment. $n = 3$ independent experiments. Statistical testing by two-way ANOVA with post hoc Tukey correction. ****$P < 0.0001$; ns, not significant. (**C**) The elevated basal DHE signal seen in LRRK2$^{GS/GS}$ HEK293 cells was unaffected by mitoTEMPO but was reduced to WT values by NAC. (**D**) Quantification of normalized DHE signal. Each symbol represents the mean normalized signal taken from 100 to 150 cells per treatment group per independent experiment. $n = 3$ independent experiments. Statistical testing by two-way ANOVA with post hoc Tukey correction. ***$P < 0.0005$; ns, not significant. (**E**) Rotenone-induced ROS production in LRRK2$^{WT/WT}$ RAW264.7 macrophages. Rotenone treatment increased the DHE signal compared with vehicle, and this was prevented by cotreatment with NOX2ds-tat but not with Scrm-NOX2ds-tat or mitoTEMPO. (**F**) Quantification of normalized DHE signal in LRRK2$^{WT/WT}$ RAW264.7 macrophages. Each symbol represents the normalized DHE signal taken from 100 to 150 cells per treatment group in each of three independent experiments. Statistical testing by two-way ANOVA with post hoc Tukey correction. ***$P < 0.001$.

B). Rotenone-induced NOX2 activation was prevented by cotreatment with PF360 and was absent in LRRK2$^{-/-}$ RAW264.7 cells (fig. S7, A and B). Rotenone treatment led to an increase in DHE signal in WT RAW264.7 macrophages ($P < 0.0005$; two-way ANOVA with Tukey correction), which was blocked by cotreatment with NOX2ds-tat (Fig. 6, E and F). Furthermore, neither mitoTEMPO nor Scrm-NOX2ds-tat prevented the increase in rotenone-induced DHE signal (Fig. 6, E and F). In control experiments, we confirmed that the increase in NOX2-derived ROS was not due to changes in NOX2 protein expression: Rotenone, PF360, and LRRK2 knockout had no effect on NOX2 and p47^{phox} protein expression (fig. S7, C to F).

We also examined whether LRRK2 regulated NOX2 activity in the in vivo rotenone rat model of PD (Fig. 4). Rotenone treatment led to a marked increase in NOX2 activity as assessed by PL p47^{phox}–NOX2 in nigral dopaminergic neurons. This was prevented by coadministration of PF360 (Fig. 7, A and B), suggesting that LRRK2 activity is upstream of NOX2 activation. To confirm the relevance of our findings, we sought to determine

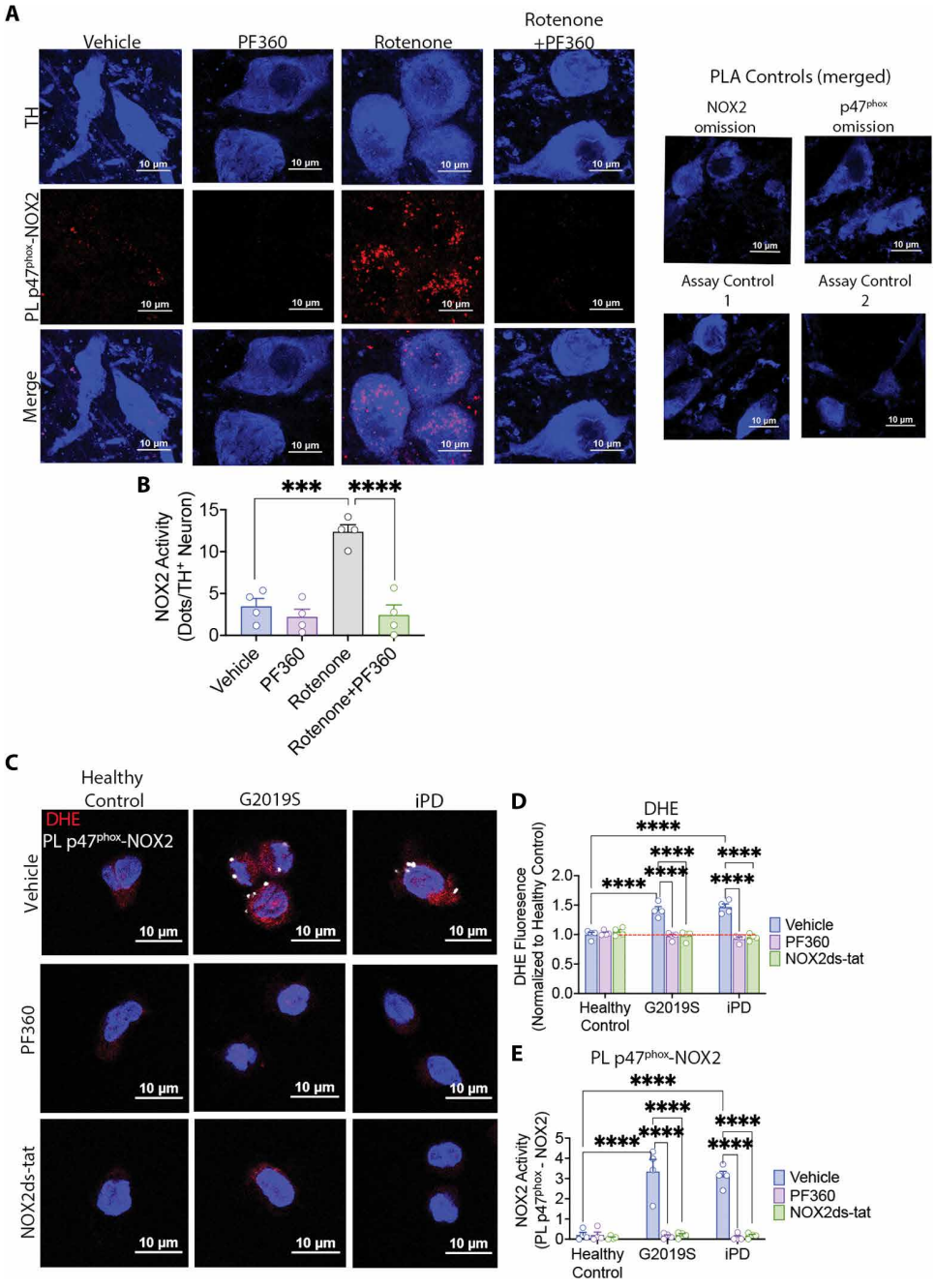

Fig. 7. LRRK2 inhibition prevents NOX2 activation in the rotenone rat model of PD and in patient-derived cell lines. (**A**) NOX2 activity was assessed by the PL p47^{phox}–NOX2 assay (red) in TH$^+$ dopaminergic neurons (blue) in the substantia nigra of rats treated with rotenone in the presence or absence of PF360. Rotenone treatment caused an increase in NOX2 activity in TH$^+$ dopaminergic neurons, and cotreatment with PF360 prevented the rotenone-induced increase in NOX2 activity. (Far right panels) Shown are PL assay tissue controls with either the NOX2 antibody or p47^{phox} antibody omitted. For assay control 1, the rabbit probe was omitted, and for assay control 2, the mouse probe was omitted. (**B**) Quantification of NOX2 activity by PL p47^{phox}–NOX2. Each symbol represents the number of PL p47^{phox}–NOX2 red dots/TH$^+$ neuron per animal. Statistical testing by two-way ANOVA with post hoc Tukey correction. ***$P < 0.0005$ and ****$P < 0.0001$. (**C**) Multiplexed imaging of ROS production assessed by DHE fluorescence (red) and NOX2 activity assessed by the PL assay (gray dots) in lymphoblastoid cell lines from healthy controls, G2019S mutation carriers, and patients with iPD. There was a coordinated increase in both DHE signal and NOX2 activity (PL p47^{phox}–NOX2 signal) in G2019S and iPD lymphoblastoid cell lines compared with healthy controls. The elevated DHE signal and NOX2 activity were reduced by treatment with either NOX2ds-tat or PF360. (**D**) Quantification of normalized DHE signal in lymphoblastoid cell lines from healthy controls, G2019S mutation carriers, and patients with iPD. Each symbol represents an individual donor cell line. DHE fluorescence signals were taken from 90 to 120 cells per line; $n = 4$ donor cell lines per group. Statistical testing by two-way ANOVA with post hoc Tukey correction. ****$P < 0.0001$. (**E**) Quantification of NOX2 activity by PL p47^{phox}–NOX2. Each symbol represents the average number of PL p47^{phox}–NOX2 gray dots per cell (as defined by DAPI staining, blue) obtained from an individual donor cell line. PL p47^{phox}–NOX2 signal was measured in 90 to 120 cells per line; $n = 4$ donor cell lines per group. Statistical testing by two-way ANOVA with post hoc Tukey correction. ****$P < 0.0001$.

whether NOX2 activity was elevated in a LRRK2 kinase–dependent manner in lymphoblastoid cell lines derived from G2019S mutation carriers and patients with iPD compared with healthy controls. Lymphoblastoid cell lines were treated with either NOX2ds-tat or PF360, and ROS production and NOX2 activity were measured by multiplexed imaging of DHE and PL p47^{phox}–NOX2. G2019S and iPD lymphoblastoid cell lines had elevated baseline DHE signals compared with healthy controls, and this was accompanied by strong PL p47^{phox}–NOX2 signals in the same cells (Fig. 7, C to E). Treatment of lymphoblastoid cell lines with NOX2ds-tat resulted in a reduction down to healthy control values of both the PL p47^{phox}–NOX2 and DHE signals in G2019S and iPD lymphoblastoid cell lines. PF360 treatment also normalized both the elevated DHE and NOX2 signals seen in the G2019S and iPD lymphoblastoid cell lines (Fig. 7, C to E). These results could not be explained by changes in NOX2 or p47^{phox} protein expression because there was a slight decrease in p47^{phox} expression in iPD compared with healthy control lymphoblastoid cell lines and no other significant differences in protein expression (fig. S8), thereby supporting the notion that the increased ROS seen in G2019S and iPD lymphoblastoid cell lines was because of elevated NOX2 enzymatic assembly and

activity, which, in turn, was regulated by mutant LRRK2 or elevated WT LRRK2 kinase activity.

Endogenous LRRK2 interacts with p47^{phox} and regulates its phosphorylation

The "organizing subunit" of NOX2, p47^{phox}, must translocate from the cytosol to the membrane-associated NOX2 complex, in a phosphorylation-dependent fashion, to activate NOX2 activity and stimulate ROS production. Several phosphorylation sites on p47^{phox} have been identified that are crucial for its translocation to the membrane. We hypothesized that there might be a link between LRRK2 kinase activity and p47^{phox} phosphorylation. First, to test whether LRRK2 and p47^{phox} interact with each other, we developed a PL assay that detected the interaction between total LRRK2 and total p47^{phox} (PL LRRK2–p47^{phox}) in RAW264.7 macrophages. Rotenone elicited a strong increase in PL LRRK2–p47^{phox} signal compared with vehicle in WT RAW264.7 macrophages ($P < 0.0001$; two-way ANOVA with Tukey correction) (Fig. 8, A and B). Consistent with the PL LRRK2–p47^{phox} results, we also found an increase in the subcellular colocalization of LRRK2 and p47^{phox} in rotenone-treated RAW264.7 macrophages (fig. S9). To investigate whether this interaction was kinase dependent, cells were cotreated with a LRRK2 kinase inhibitor. PF360 prevented the rotenone-induced PL LRRK2–p47^{phox} signal ($P < 0.0001$; two-way ANOVA with Tukey correction) (Fig. 8, A and B), suggesting that the interaction was dependent on LRRK2 kinase activity. In control experiments, we did not observe a PL LRRK2–p47^{phox} signal in LRRK2$^{-/-}$ RAW264.7 macrophages (Fig. 8, A and B).

The Ser^{345} residue on p47^{phox}, pSer^{345}(p47^{phox}), has been shown to be an important phosphorylation site for NOX2 activation (*10*, *28*). Thus, we next assessed pSer^{345}(p47^{phox}) after treatment with rotenone to determine whether LRRK2 kinase activity played a role in regulating its phosphorylation. We developed another PL assay to amplify the specific signal at pSer^{345}(p47^{phox}) (PL pSer^{345}–total p47^{phox}). We used a validated and specific anti-pSer^{345}(p47^{phox}) antibody paired with an antibody that recognizes total p47^{phox}. This allowed for the signal of pSer^{345} to be detected only if it was in proximity to p47^{phox}, thereby filtering out any nonspecific pSer^{345} signal. Using this assay, we found an increase in the PL pSer^{345}–total p47^{phox} signal in WT RAW264.7 macrophages treated with rotenone ($P < 0.0001$; two-way ANOVA with Tukey correction) (Fig. 8, C and D), which confirms previous findings from an independent group (*29*). Similarly, in rotenone-treated rats, there was an increase in the PL pSer^{345}–total p47^{phox} signal in nigral dopaminergic neurons compared with vehicle ($P < 0.05$, two tailed unpaired *t* test with Welch's correction) (fig. S10).

We sought to determine whether LRRK2 played a role in regulating rotenone-induced p47^{phox} phosphorylation at Ser^{345}. Intriguingly, cotreatment with PF360 blocked the effects of rotenone on Ser^{345}(p47^{phox}) phosphorylation ($P < 0.0001$; two-way ANOVA with Tukey correction) (Fig. 8, C and D). In rotenone-treated LRRK2$^{-/-}$ RAW264.7 macrophages, no PL pSer^{345}–total p47^{phox} signal was detected (Fig. 8, C and D), confirming both PF360's specificity and a role for LRRK2 in regulating the phosphorylation of p47^{phox}. Supporting this finding, immunofluorescent staining for pSer^{345}(p47^{phox}) revealed an increase in pSer^{345}(p47^{phox}) signal in WT RAW264.7 macrophages treated with rotenone ($P < 0.005$; two-way ANOVA with Tukey correction) (fig. S11). In WT RAW264.7 macrophages cotreated with PF360 and rotenone, or in LRRK2$^{-/-}$ RAW264.7 macrophages treated with rotenone, no increase in pSer^{345}(p47^{phox}) immunoreactivity was detected (fig. S11).

Ser^{345}(p47^{phox}) is located in a consensus mitogen-activated protein kinase (MAPK) motif, and two MAPKs, p38 and ERK1/2, have been shown to phosphorylate it (*30*). Therefore, we sought to determine whether pSer^{345}(p47^{phox}) was under the direct regulation of p38 or ERK1/2 kinase activity. We used the specific p38 and ERK1/2 inhibitors, adezmapimod (*31*) and SCH772984 (*32*), respectively, each at saturating concentration. In contrast to PF360, which completely suppressed rotenone induced Ser^{345} phosphorylation, adezmapimod or SCH772984, alone or in combination, only partially blocked the effect of rotenone on pSer^{345}(p47^{phox}) in WT RAW264.7 macrophages (Fig. 8, E and F).

DISCUSSION

Oxidative stress has long been implicated as a key contributor to PD pathogenesis (*2*); however, the sources and regulation of ROS have yet to be adequately defined. Whereas overexpression of mutant LRRK2 has been associated with oxidative stress (*24*, *25*), the responsible mechanisms are unknown. Moreover, the biological functions of LRRK2 and how the mutant and WT forms of the protein participate in the pathogenesis of PD are still being elucidated. Here, we used several in vitro cellular models (CRISPR-Cas9 gene-edited HEK293 cells, WT and *LRRK2*$^{-/-}$ RAW264.7 macrophages, primary rat nigral dopaminergic neurons), an in vivo rat model of PD, and patient-derived lymphoblastoid cell lines to show that endogenous LRRK2 kinase activity regulates the phosphorylation status of p47^{phox}, which in turn controls NOX2 activity, ROS production, and oxidative damage, including lipid peroxidation (fig. S12).

When investigating protein function or protein-protein interactions, overexpression systems are commonly used. It is recognized, however, that overexpression can sometimes be associated with spurious protein-protein interactions or other artifacts (*33*, *34*). Therefore, in the work presented here, we endeavored to study WT and mutant LRRK2 in an endogenous context and aimed to use orthogonal assays to support each conclusion. WT and mutant LRRK2 (G2019S and R1441G mutations) were studied in gene-edited HEK293 cells, and WT LRRK2 kinase activity was stimulated with rotenone. LRRK2 kinase activity was assessed both by PL assay, as described previously (*18*, *35*), and by Western blotting of substrate (Rab10) phosphorylation. LRRK2 kinase dependence was assessed by genetic (knockout) and pharmacological (PF360 and MLi2) approaches. Cellular ROS production was measured using DHE and was correlated with an independent measure of oxidative damage, lipid peroxidation, using 4-HNE staining.

We found that under basal conditions, cells expressing endogenous LRRK2$^{GS/GS}$ had elevated ROS production and 4-HNE accumulation, both of which were LRRK2 kinase dependent. As a complex I inhibitor, rotenone is well known to cause ROS production (*7*), and, as expected, when WT HEK293 cells or RAW264.7 macrophages were stimulated with rotenone, there was enhanced ROS production and oxidative damage. Unexpectedly, however, treatment with a LRRK2 kinase inhibitor blocked rotenone-induced ROS and 4-HNE accumulation, and genetic knockout of LRRK2 completely prevented rotenone-induced ROS production and oxidative damage in multiple cell types, including macrophages. When LRRK2$^{-/-}$ cells were transfected with WT-LRRK2, only those cells that expressed WT LRRK2 were sensitive to rotenone, whereas

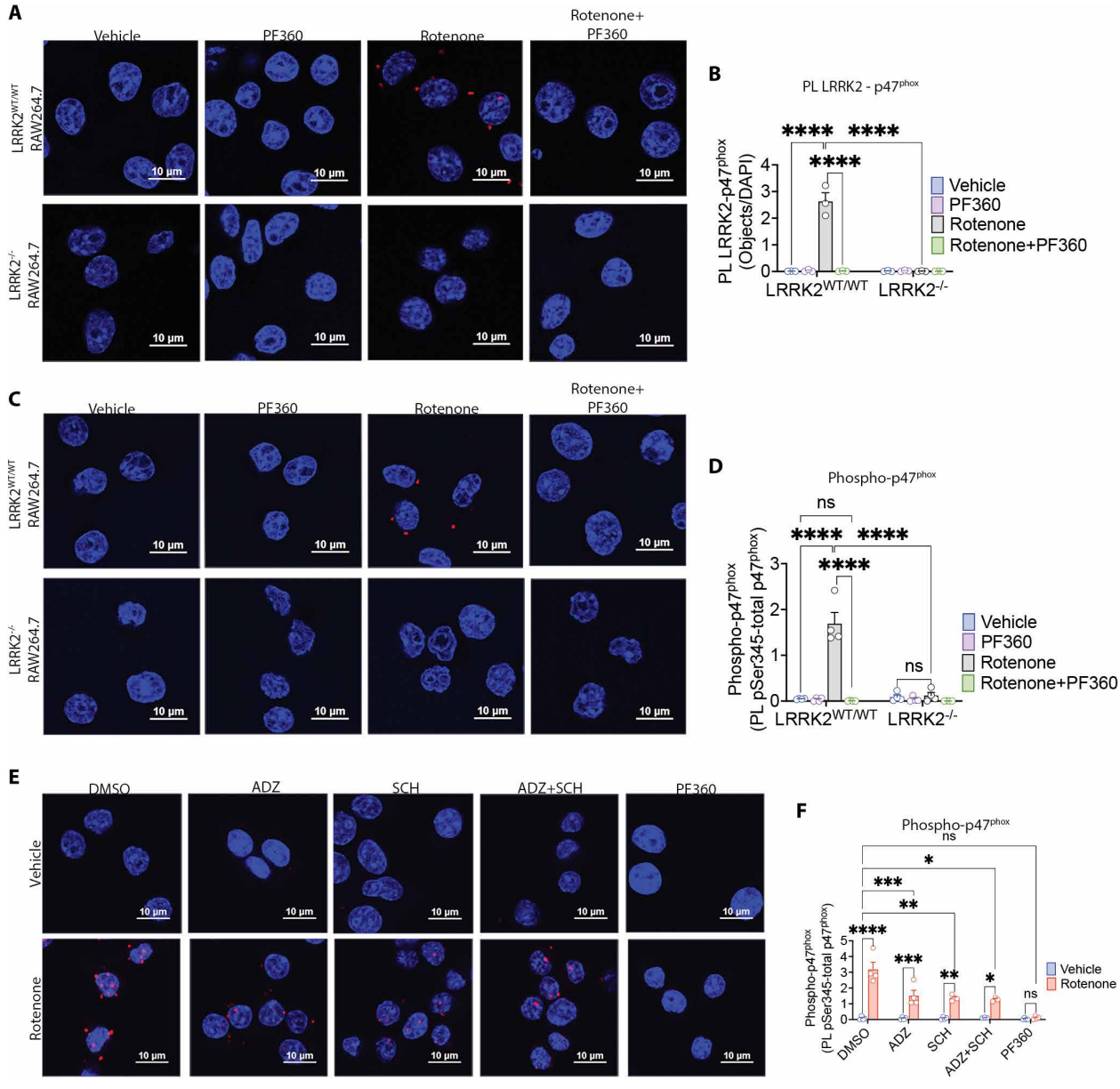

Fig. 8. Endogenous LRRK2 interacts with p47^{phox} and regulates its phosphorylation in a kinase-dependent manner. (**A**) A PL assay was used to measure the interaction of LRRK2 and p47^{phox} (PL LRRK2–p47^{phox}) in LRRK2$^{WT/WT}$ and LRRK2$^{-/-}$ RAW264.7 macrophages. Exposure of LRRK2$^{WT/WT}$ cells to rotenone caused a strong signal (red dots) relative to vehicle in this assay. The rotenone-induced PL LRRK2–p47^{phox} signal was prevented by cotreatment with PF360 and was not observed in LRRK2$^{-/-}$ cells. (**B**) Quantification of PL LRRK2–p47^{phox} signal. Each symbol represents the average number of PL LRRK2–p47^{phox} red dots per cell (as defined by DAPI staining, blue) obtained from 100 to 150 cells per treatment group for each independent experiment. $n = 4$ independent experiments. Statistical testing by two-way ANOVA with post hoc Tukey correction. ****$P < 0.0001$; ns, not significant. (**C**) Phosphorylation of p47phox at serine-345, pSer^{345}(p47^{phox}), was assessed using the PL assay in LRRK2$^{WT/WT}$ and LRRK2$^{-/-}$ RAW264.7 macrophages. Rotenone treatment led to an increase in pSer^{345}(p47^{phox}) in LRRK2$^{WT/WT}$ cells as measured by the pSer^{345}–total p47^{phox} signal (red dots). PF360 cotreatment prevented the rotenone-induced increase in pSer^{345}(p47^{phox}) signal, and the signal was absent in LRRK2$^{-/-}$ cells. (**D**) Quantification of the pSer^{345}–total p47^{phox} signal in RAW264.7 macrophages. Each symbol represents the average number of red dots per cell (as defined by DAPI staining, blue) obtained from 100 to 150 cells per treatment group for each experiment. $n = 4$ independent experiments. Statistical testing by two-way ANOVA with post hoc Tukey correction. ****$P < 0.0001$; ns, not significant. (**E**) Rotenone-induced pSer^{345}–total p47^{phox} signal was assessed in the presence of PF360, the p38 kinase inhibitor adezmapimod (5 µM; ADZ), the ERK1/2 inhibitor SCH772984 (300 nM; SCH), or both kinase inhibitors in combination. Rotenone treatment elicited an increase in pSer^{345}–total p47^{phox} signal (red dots), which was abolished by PF360 cotreatment. In contrast to PF360, ADZ or SCH alone or in combination (ADZ + SCH) only partially reduced the rotenone-induced pSer^{345}–total p47^{phox} signal. (**F**) Shown is quantitation of the pharmacological inhibition of the rotenone-induced increase in pSer^{345}–total p47^{phox} signal. Each symbol represents the average number of pSer^{345}–total p47^{phox} red dots per cell (as defined by DAPI staining, blue) obtained from 100 to 150 cells per treatment group for each experiment. $n = 3$ or 4 independent experiments. Statistical testing by two-way ANOVA with post hoc Tukey correction. ****$P < 0.0001$, ***$P < 0.001$, **$P < 0.005$, and *$P < 0.05$; ns, not significant.

other cells in the same field that did not express LRRK2 exhibited no rotenone-induced ROS production. These results suggest a conserved role for LRRK2 in regulating cellular ROS production. Our findings are consistent with a previous report that knockdown of endogenous LRRK2 in RAW264.7 macrophages attenuated interferon-γ–stimulated ROS production (*36*), although no mechanism was described. Similarly, a recent publication found that LRRK2 knockout was sufficient to prevent rotenone-induced ROS production; however, that study used a very high concentration of rotenone (50 μM compared with 50 nM herein), and no mechanism was advanced (*37*).

After defining a putative role for LRRK2 in regulating ROS production in HEK293 cells and RAW264.7 macrophages, we next investigated the relevance of our findings in a neuronal context using primary rat ventral midbrain cultures and an in vivo rat model. Treatment of primary cultures with rotenone caused accumulation of 4-HNE selectively in dopamine neurons, and this was prevented by cotreatment with a LRRK2 inhibitor. Similarly, in the in vivo rotenone rat model of PD (*23*), we found a marked loss of substantia nigra dopamine neurons and a buildup of 4-HNE in the remaining dopamine neurons in rotenone-treated animals. Both the lipid peroxidation and neurodegeneration of dopamine neurons were prevented by coadministration of a LRRK2 inhibitor, thereby confirming the in vivo and neuronal relevance of LRRK2-induced ROS production. Last, to examine whether LRRK2-induced ROS production occurs in human PD, we used lymphoblastoid cell lines derived from healthy controls, LRRK2 G2019S mutation carriers, and individuals with iPD. Compared with healthy controls, lymphoblastoid cell lines derived from both the mutation carriers and patients with iPD had elevated ROS production and 4-HNE, which was blocked by two structurally dissimilar LRRK2 kinase inhibitors, PF360 and MLi2. Collectively, these findings implicate a role for endogenous aberrant LRRK2 kinase activity in the regulation of ROS production and oxidative stress.

To investigate how LRRK2 regulates ROS production, we examined the potential role of LRRK2 in modulating the major sources of ROS found in most cells: mitochondria and NOX2. The relative contribution and regulation of each source of ROS has yet to be elucidated. There are reports that G2019S LRRK2 kinase activity leads to mitochondrial dysfunction, lipid peroxidation, and mitochondrial ROS production (*38*–*41*). We found that the LRRK2 pathogenic mutations G2019S and R1441G, each of which is associated with increased kinase activity, caused enhanced mitochondrial ROS production, which could be inhibited by a LRRK2 kinase inhibitor or by mitoTEMPO, a mitochondrial ROS scavenger. The combined use of these cells expressing mutant LRRK2, which have elevated kinase activity at baseline (without rotenone stimulation), in conjunction with a highly selective LRRK2 kinase inhibitor allowed us to conclude that it is LRRK2 kinase activity per se that is somehow responsible for the elevated mitochondrial ROS production.

LRRK2 kinase activity also regulates NOX2 activity. In G2019S mutant LRRK2 knockin cells, we found that under basal conditions, there was elevated NOX2 activity that was blocked by LRRK2 kinase inhibition but unaffected by scavenging mitochondrial ROS. This suggested that kinase-active LRRK2 plays a role in the activation of NOX2, independent of mitochondrial ROS production. Moreover, G2019S-associated or rotenone-induced ROS production and 4-HNE accumulation in LRRK2$^{GS/GS}$ HEK293 cells or LRRK2$^{WT/WT}$ RAW264.7 macrophages were prevented by inhibition of NOX2 or LRRK2 but not by mitoTEMPO. In vivo results in a rat PD model also support the regulation of NOX2 by LRRK2. As previously reported, treatment of rats with rotenone activates NOX2 in dopaminergic neurons of the substantia nigra (*12*). Here, we showed that rotenone-induced NOX2 activation was prevented in animals coadministered PF360. Moreover, we demonstrated elevated basal ROS production and NOX2 activity in G2019S and iPD patient–derived lymphoblastoid cell lines, compared with those from healthy controls, both of which were normalized by either NOX2 or LRRK2 inhibition. We propose from these results that NOX2 is the major source of cellular ROS and is regulated by LRRK2 kinase activity.

A key step in the assembly and activation of the membrane-associated NOX2 complex is the phosphorylation of p47^{phox}, a cytosolic protein sometimes called the organizing subunit of NOX2 (*10*, *11*). Several phosphorylation sites have been identified that are crucial for its translocation to the membrane-associated gp91^{phox} (NOX2) subunit, which results in NOX2 enzyme activation and subsequent superoxide production (*9*, *11*). Ser^{345} has been shown to be an important phosphorylation site for NOX2 activation, because site-directed mutagenesis experiments showed that when it was mutated to an alanine, stimulated NOX2 ROS production was prevented (*28*, *30*, *42*). We found that rotenone treatment, which causes NOX2 activation, led to an interaction between LRRK2 and p47^{phox} in LRRK2$^{WT/WT}$ RAW264.7 macrophages, which was prevented by LRRK2 kinase inhibition. Furthermore, rotenone treatment induced an increase in phosphorylation of Ser^{345}, consistent with a previous report (*29*). The rotenone-induced increase in Ser^{345} phosphorylation was blocked by LRRK2 inhibition and completely prevented by LRRK2 knockout. ERK1/2 and p38 have been shown to play a role in the phosphorylation of p47^{phox} at Ser^{345} (*30*), and there is evidence that rotenone activates the ERK1/2 and p38 pathways (*29*, *43*). However, we found that inhibition of ERK1/2 and p38 individually, or in combination, only partially reduced rotenone-induced Ser^{345} phosphorylation; this was in contrast to LRRK2 inhibition, which completely eliminated pSer^{345} signal. Together, these results show that LRRK2 associates with p47^{phox} in a kinase-dependent fashion and regulates its phosphorylation state, thereby regulating NOX2 activity and cellular ROS production. We note that there is precedent for a functional interaction between LRRK2 and NOX2: Knockdown of p22^{phox}, a component of the active NOX2 complex, reportedly prevented the recruitment of LRRK2 to lysosomes (*44*).

Our study has several limitations. We have not determined how elevated LRRK2 kinase activity increases mitochondrial ROS production, but we note that our results are consistent with a recent report (*45*) implicating LRRK2 kinase activity in mtDNA damage. In addition, although we have provided evidence that LRRK2 associates with and regulates the phosphorylation state of p47^{phox} and hence NOX2 activity, we do not know whether p47^{phox} is a direct substrate of LRRK2. Moreover, other than mitochondria, we have not yet determined the subcellular locations of LRRK2-induced ROS production. Last, given the importance of LRRK2 and NOX2 in immune function, it will be important to investigate the role of LRRK2-induced ROS production in microglia.

In summary, we have delineated a role for LRRK2 kinase activity in the regulation of cellular ROS production and shown the pathogenic relevance of LRRK2-induced ROS production in neurons and macrophages in vitro, in a rat model of PD and in patient-derived lymphoblastoid cell lines. The associated overactivation of NOX2

may directly increase the vulnerability of neurons (especially nigral dopamine neurons) and may exacerbate α-synuclein pathology or pathobiology (*12*, *18*, *46*). Last, given the strong lipid peroxidation induced by LRRK2 kinase activity, this work raises the possibility that oxidized lipidomic analyses (*47*, *48*) might reveal a marker for therapeutic target engagement or efficacy of LRRK2 or NOX2 inhibitors.

MATERIALS AND METHODS

Study design

This study was designed to explore the role LRRK2 kinase activity plays in regulating ROS production and oxidative damage. To this end, we used CRISPR-Cas9 gene-edited HEK293 cells, RAW264.7 macrophages, primary cultures of rat ventral midbrain neurons, patient-derived lymphoblastoid cell lines, and an in vivo rotenone rat model of PD to explore whether elevated LRRK2 kinase activity controls ROS production and, if so, how this occurs. To enhance scientific rigor, we generally used orthogonal approaches to support each conclusion, and, in some cases, we used both specific pharmacological inhibitors and genetic knockout approaches to support key findings. Results were confirmed in patient-derived lymphoblastoid cell lines and in an in vivo rat model of PD. To ensure reproducibility, all in vitro experiments were replicated independently at least three times, typically by two or three investigators for each dataset. Investigators were not blinded during experimental setup or data acquisition. In vivo experiments were conducted using a single cohort of rats that were assigned randomly to treatment groups, and outcomes were analyzed by blinded assessors. No animals were excluded from analysis, and there were no statistical outliers.

Cell culture

HEK293 cells and RAW264.7 macrophages were cultured in DMEM/F12 (Thermo Fisher Scientific) supplemented with 10% fetal bovine serum (FBS) and penicillin-streptomycin (pen-strep). Cells were maintained at 37°C and 5% CO_2. CRISPR-Cas9 gene-edited HEK293 cells were generated as previously described (*18*). LRRK2$^{-/-}$ (sc-6004) and LRRK2$^{WT/WT}$ (parental) (sc-6003) RAW264.7 macrophages were obtained from American Type Culture Collection. Cell passage number did not exceed 20 for HEK293 cells or RAW264.7 macrophages. Patient-derived lymphoblastoid cell lines were obtained from the NINDS Coriell Biorepository through a material transfer agreement, and sample identification numbers may be found in table S1. Cells were maintained in RPMI medium GlutaMAX supplement (Thermo Fisher Scientific) with 15% FBS and pen-strep. Cells were plated on poly-D-lysine–coated coverslips in a 24-well plate or 16-well Nunc Lab Tek chamber slides (Thermo Fisher Scientific) and attached by light centrifugation at 690*g* at room temperature. Cells were passaged every 3 days and did not exceed 20 passages. Rat primary ventral midbrain neuronal cultures were maintained as previously described (*12*). Details for reagents used for cell treatments can be found in table S2.

Animals

All experiments using animals were approved by the Institutional Animal Care and Use Committee of the University of Pittsburgh. Male Lewis rats (8 to 9 months old) received a single daily intraperitoneal injection of rotenone (2.8 mg/kg) resuspended in 2% dimethyl sulfoxide (DMSO) and 98% miglyol 812 N as previously described (*23*, *49*) with or without PF360 (5 mg/kg, oral gavage, twice daily) until they reached a behavioral end point (7 to 10 injections). Animals were euthanized using pentobarbital (0.3 mg/kg), followed by transcardial perfusion. Brains were removed and post-fixed in 4% paraformaldehyde for 24 hours before placing them in 30% sucrose. Free-floating sections (35 μm) were collected using a microtome and stored in cryoprotectant at −20°C until use.

PL assay

Cells

PL assay was performed in 16-well Nunc Lab Tek chamber slides (Thermo Fisher Scientific) using a NaveniFlex MR Kit (catalog no. NF.MR.100, Navinci). Cells were fixed, blocked/permeabilized, and incubated in primary antibody solution as previously described (*35*). After overnight primary antibody incubation, cells underwent three 10-min washes in phosphate-buffered saline (PBS). After washes, the proximity ligation assay was performed according to the manufacturer's instructions (Navinci.se) with modifications outlined in (*35*), with the incubation steps taking place in a humidified incubator at 37°C with gentle agitation, taking care that samples did not dry out. For details of other products used, see (*35*).

Brain tissue

PL assay was performed in blocked and permeabilized brain tissue as previously described (*35*) using the NaveniFlex MR Kit (Navinci). After overnight primary antibody incubation, tissue sections underwent three 10-min washes in PBS and then were mounted on glass slides (Thermo Fisher Scientific). See (*35*) for detailed description and video of mounting of tissue before PL assay. The PL assay was performed according to the manufacturer's instructions (Navinci.se) with modifications outlined in (*35*); incubation steps took place at 37°C ensuring that samples did not dry out. After completion of the PL assay, sections were covered with a glass coverslip with gelvatol mounting medium.

mitoSOX–deep red assay

mitoSOX–deep red (catalog no. MUT14-12) was purchased from Dojindo. Before each use, a vial of mitoSOX–deep red was briefly spun down and reconstituted in 10 μl of DMSO per the manufacturer's instructions. Cells were plated on a 35-mm glass bottom dish coated with poly-D-lysine and treated with vehicle, PF360, MLi2, or mitoTEMPO (see table S1 for concentrations) for 24 hours in normal growth medium. The following day, the cells were incubated in 2 ml of growth medium containing mitoSOX–deep red (1:1000 dilution) for 30 min at 37°C and 5% CO_2. After incubation, cells were washed with Earle's balanced salt solution (EBSS) two times. EBBS with 4′,6-diamidino-2-phenylindole (DAPI) was added to each 35-mm plate and incubated for 5 min at 37°C and 5% CO_2 followed by a wash with EBSS. Cells were then imaged on a Nikon Eclipse Ti2 resonance scan spectral confocal microscope.

Statistical analysis

Sample sizes were estimated from our recent publications and preliminary studies. In general, a sample size of three to six per group is sufficient to detect differences of 20% in the outcome variables to be used. Results are presented as mean ± SEM and were derived from three or four independent experiments. For comparisons of multiple experimental conditions, one-way or two-way ANOVA was used, and, if significant overall, post hoc corrections (with Tukey tests) for multiple comparisons were made. *P* values less than 0.05 were considered significant.

Supplementary Materials

The PDF file includes:
Materials and Methods
Figs. S1 to S12
Tables S1 to S3
Reference (*50*)

Other Supplementary Material for this manuscript includes the following:
Data file S1
MDAR Reproducibility Checklist

REFERENCES AND NOTES

1. L. V. Kalia, A. E. Lang, Parkinson's disease. *Lancet* **386**, 896–912 (2015).
2. V. Dias, E. Junn, M. M. Mouradian, The role of oxidative stress in Parkinson's disease. *J. Parkinsons Dis.* **3**, 461–491 (2013).
3. A. Yoritaka, N. Hattori, K. Uchida, M. Tanaka, E. R. Stadtman, Y. Mizuno, Immunohistochemical detection of 4-hydroxynonenal protein adducts in Parkinson disease. *Proc. Natl. Acad. Sci. U.S.A.* **93**, 2696–2701 (1996).
4. Z. I. Alam, S. E. Daniel, A. J. Lees, D. C. Marsden, P. Jenner, B. Halliwell, A generalised increase in protein carbonyls in the brain in Parkinson's but not incidental Lewy body disease. *J. Neurochem.* **69**, 1326–1329 (1997).
5. J. Sian, D. T. Dexter, A. J. Lees, S. Daniel, Y. Agid, F. Javoy-Agid, P. Jenner, C. D. Marsden, Alterations in glutathione levels in Parkinson's disease and other neurodegenerative disorders affecting basal ganglia. *Ann. Neurol.* **36**, 348–355 (1994).
6. A. H. Schapira, J. M. Cooper, D. Dexter, J. B. Clark, P. Jenner, C. D. Marsden, Mitochondrial complex I deficiency in Parkinson's disease. *J. Neurochem.* **54**, 823–827 (1990).
7. J. T. Greenamyre, T. B. Sherer, R. Betarbet, A. V. Panov, Complex I and Parkinson's disease. *IUBMB Life* **52**, 135–141 (2001).
8. S. Dikalov, Cross talk between mitochondria and NADPH oxidases. *Free Radic. Biol. Med.* **51**, 1289–1301 (2011).
9. K. Bode, M. Hauri-Hohl, V. Jaquet, H. Weyd, Unlocking the power of NOX2: A comprehensive review on its role in immune regulation. *Redox Biol.* **64**, 102795 (2023).
10. J. El-Benna, P. M. Dang, M. A. Gougerot-Pocidalo, J. C. Marie, F. Braut-Boucher, p47phox, The phagocyte NADPH oxidase/NOX2 organizer: Structure, phosphorylation and implication in diseases. *Exp. Mol. Med.* **41**, 217–225 (2009).
11. D. Rotrosen, T. L. Leto, Phosphorylation of neutrophil 47-kDa cytosolic oxidase factor. Translocation to membrane is associated with distinct phosphorylation events. *J. Biol. Chem.* **265**, 19910–19915 (1990).
12. M. T. Keeney, E. K. Hoffman, K. Farmer, C. R. Bodle, M. Fazzari, A. Zharikov, S. L. Castro, X. Hu, A. Mortimer, J. K. Kofler, E. Cifuentes-Pagano, P. J. Pagano, E. A. Burton, T. G. Hastings, J. T. Greenamyre, R. di Maio, NADPH oxidase 2 activity in Parkinson's disease. *Neurobiol. Dis.* **170**, 105754 (2022).
13. E. M. Rocha, M. T. Keeney, R. Di Maio, B. R. De Miranda, J. T. Greenamyre, LRRK2 and idiopathic Parkinson's disease. *Trends Neurosci.* **45**, 224–236 (2022).
14. A. Zimprich, S. Biskup, P. Leitner, P. Lichtner, M. Farrer, S. Lincoln, J. Kachergus, M. Hulihan, R. J. Uitti, D. B. Calne, A. J. Stoessl, R. F. Pfeiffer, N. Patenge, I. C. Carbajal, P. Vieregge, F. Asmus, B. Müller-Myhsok, D. W. Dickson, T. Meitinger, T. M. Strom, Z. K. Wszolek, T. Gasser, Mutations in LRRK2 cause autosomal-dominant parkinsonism with pleomorphic pathology. *Neuron* **44**, 601–607 (2004).
15. C. Paisan-Ruiz, S. Jain, E. W. Evans, W. P. Gilks, J. Simón, M. van der Brug, A. L. de Munain, S. Aparicio, A. M. Gil, N. Khan, J. Johnson, J. R. Martinez, D. Nicholl, I. M. Carrera, A. S. Pena, R. de Silva, A. Lees, J. F. Martí-Massó, J. Pérez-Tur, N. W. Wood, A. B. Singleton, Cloning of the gene containing mutations that cause PARK8-linked Parkinson's disease. *Neuron* **44**, 595–600 (2004).
16. E. Greggio, S. Jain, A. Kingsbury, R. Bandopadhyay, P. Lewis, A. Kaganovich, M. P. van der Brug, A. Beilina, J. Blackinton, K. J. Thomas, R. Ahmad, D. W. Miller, S. Kesavapany, A. Singleton, A. Lees, R. J. Harvey, K. Harvey, M. R. Cookson, Kinase activity is required for the toxic effects of mutant LRRK2/dardarin. *Neurobiol. Dis.* **23**, 329–341 (2006).
17. L. Petropoulou-Vathi, A. Simitsi, P. E. Valkimadi, M. Kedariti, L. Dimitrakopoulos, C. Koros, D. Papadimitriou, A. Papadimitriou, L. Stefanis, R. N. Alcalay, H. J. Rideout, Distinct profiles of LRRK2 activation and Rab GTPase phosphorylation in clinical samples from different PD cohorts. *NPJ Parkinsons Dis.* **8**, 73 (2022).
18. R. Di Maio, E. K. Hoffman, E. M. Rocha, M. T. Keeney, L. H. Sanders, B. R. De Miranda, A. Zharikov, A. Van Laar, A. F. Stepan, T. A. Lanz, J. K. Kofler, E. A. Burton, D. R. Alessi, T. G. Hastings, J. T. Greenamyre, LRRK2 activation in idiopathic Parkinson's disease. *Sci. Transl. Med.* **10**, eaar5429 (2018).
19. K. B. Fraser, A. B. Rawlins, R. G. Clark, R. N. Alcalay, D. G. Standaert, N. Liu; Parkinson's Disease Biomarker Program Consortium, A. B. West, Ser(P)-1292 LRRK2 in urinary exosomes is elevated in idiopathic Parkinson's disease. *Mov. Disord.* **31**, 1543–1550 (2016).
20. D. Jennings, S. Huntwork-Rodriguez, A. G. Henry, J. C. Sasaki, R. Meisner, D. Diaz, H. Solanoy, X. Wang, E. Negrou, V. V. Bondar, R. Ghosh, M. T. Maloney, N. E. Propson, Y. Zhu, R. D. Maciuca, L. Harris, A. Kay, P. LeWitt, T. A. King, D. Kern, A. Ellenbogen, I. Goodman, A. Siderowf, J. Aldred, O. Omidvar, S. T. Masoud, S. S. Davis, A. Arguello, A. A. Estrada, J. de Vicente, Z. K. Sweeney, G. Astarita, M. T. Borin, B. K. Wong, H. Wong, H. Nguyen, K. Scearce-Levie, C. Ho, M. D. Troyer, Preclinical and clinical evaluation of the LRRK2 inhibitor DNL201 for Parkinson's disease. *Sci. Transl. Med.* **14**, eabj2658 (2022).
21. J. P. Daher, L. A. Volpicelli-Daley, J. P. Blackburn, M. S. Moehle, A. B. West, Abrogation of α-synuclein-mediated dopaminergic neurodegeneration in LRRK2-deficient rats. *Proc. Natl. Acad. Sci. U.S.A.* **111**, 9289–9294 (2014).
22. J. P. L. Daher, H. A. Abdelmotilib, X. Hu, L. A. Volpicelli-Daley, M. S. Moehle, K. B. Fraser, E. Needle, Y. Chen, S. J. Steyn, P. Galatsis, W. D. Hirst, A. B. West, Leucine-rich repeat kinase 2 (LRRK2) pharmacological inhibition abates α-synuclein gene-induced neurodegeneration. *J. Biol. Chem.* **290**, 19433–19444 (2015).
23. E. M. Rocha, B. R. de Miranda, S. Castro, R. Drolet, N. G. Hatcher, L. Yao, S. M. Smith, M. T. Keeney, R. di Maio, J. Kofler, T. G. Hastings, J. T. Greenamyre, LRRK2 inhibition prevents endolysosomal deficits seen in human Parkinson's disease. *Neurobiol. Dis.* **134**, 104626 (2020).
24. D. Yang, T. Li, Z. Liu, N. Arbez, J. Yan, T. H. Moran, C. A. Ross, W. W. Smith, LRRK2 kinase activity mediates toxic interactions between genetic mutation and oxidative stress in a *Drosophila* model: Suppression by curcumin. *Neurobiol. Dis.* **47**, 385–392 (2012).
25. J. Zhang, K. Li, X. Wang, A. M. Smith, B. Ning, Z. Liu, C. Liu, C. A. Ross, W. W. Smith, Curcumin reduced H_2O_2- and G2385R-LRRK2-induced neurodegeneration. *Front. Aging Neurosci.* **13**, 754956 (2021).
26. F. E. Rey, M. E. Cifuentes, A. Kiarash, M. T. Quinn, P. J. Pagano, Novel competitive inhibitor of NAD(P)H oxidase assembly attenuates vascular O_2^- and systolic blood pressure in mice. *Circ. Res.* **89**, 408–414 (2001).
27. G. Csanyi, E. Cifuentes-Pagano, I. A. Ghouleh, D. J. Ranayhossaini, L. Egaña, L. R. Lopes, H. M. Jackson, E. E. Kelley, P. J. Pagano, Nox2 B-loop peptide, Nox2ds, specifically inhibits the NADPH oxidase Nox2. *Free Radic. Biol. Med.* **51**, 1116–1125 (2011).
28. L. Teng, L. M. Fan, D. Meijles, J. M. Li, Divergent effects of $p47^{phox}$ phosphorylation at S303-4 or S379 on tumor necrosis factor-α signaling via TRAF4 and MAPK in endothelial cells. *Arterioscler. Thromb. Vasc. Biol.* **32**, 1488–1496 (2012).
29. X. Zhang, D. Tu, S. Li, N. Li, D. Li, Y. Gao, L. Tian, J. Liu, X. Zhang, J. S. Hong, L. Hou, J. Zhao, Q. Wang, A novel synthetic peptide SVHRSP attenuates dopaminergic neurodegeneration by inhibiting NADPH oxidase-mediated neuroinflammation in experimental models of Parkinson's disease. *Free Radic. Biol. Med.* **188**, 363–374 (2022).
30. P. M. Dang, A. Stensballe, T. Boussetta, H. Raad, C. Dewas, Y. Kroviarski, G. Hayem, O. N. Jensen, M. A. Gougerot-Pocidalo, J. el-Benna, A specific p47phox-serine phosphorylated by convergent MAPKs mediates neutrophil NADPH oxidase priming at inflammatory sites. *J. Clin. Invest.* **116**, 2033–2043 (2006).
31. S. P. Davies, H. Reddy, M. Caivano, P. Cohen, Specificity and mechanism of action of some commonly used protein kinase inhibitors. *Biochem. J.* **351**, 95–105 (2000).
32. E. J. Morris, S. Jha, C. R. Restaino, P. Dayananth, H. Zhu, A. Cooper, D. Carr, Y. Deng, W. Jin, S. Black, B. Long, J. Liu, E. DiNunzio, W. Windsor, R. Zhang, S. Zhao, M. H. Angagaw, E. M. Pinheiro, J. Desai, L. Xiao, G. Shipps, A. Hruza, J. Wang, J. Kelly, S. Paliwal, X. Gao, B. S. Babu, L. Zhu, P. Daublain, L. Zhang, B. A. Lutterbach, M. R. Pelletier, U. Philippar, P. Siliphaivanh, D. Witter, P. Kirschmeier, W. R. Bishop, D. Hicklin, D. G. Gilliland, L. Jayaraman, L. Zawel, S. Fawell, A. A. Samatar, Discovery of a novel ERK inhibitor with activity in models of acquired resistance to BRAF and MEK inhibitors. *Cancer Discov.* **3**, 742–750 (2013).
33. S. Barth, D. Glick, K. F. Macleod, Autophagy: Assays and artifacts. *J. Pathol.* **221**, 117–124 (2010).
34. N. Watamura, K. Sato, T. C. Saido, Mouse models of Alzheimer's disease for preclinical research. *Neurochem. Int.* **158**, 105361 (2022).
35. M. T. Keeney, E. K. Hoffman, T. J. Greenamyre, R. Di Maio, Measurement of LRRK2 kinase activity by proximity ligation assay. *Bio. Protoc.* **11**, e4140 (2021).
36. A. Gardet, Y. Benita, C. Li, B. E. Sands, I. Ballester, C. Stevens, J. R. Korzenik, J. D. Rioux, M. J. Daly, R. J. Xavier, D. K. Podolsky, LRRK2 is involved in the IFN-γ response and host response to pathogens. *J. Immunol.* **185**, 5577–5585 (2010).
37. D. A. Quintero-Espinosa, S. Sanchez-Hernandez, C. Velez-Pardo, F. Martin, M. Jimenez-Del-Rio, LRRK2 knockout confers resistance in HEK-293 cells to rotenone-induced oxidative stress, mitochondrial damage, and apoptosis. *Int. J. Mol. Sci.* **24**, 10474 (2023).
38. H. Mortiboys, K. K. Johansen, J. O. Aasly, O. Bandmann, Mitochondrial impairment in patients with Parkinson disease with the G2019S mutation in LRRK2. *Neurology* **75**, 2017–2020 (2010).
39. M. G. Williamson, M. Madureira, W. McGuinness, R. Heon-Roberts, E. D. Mock, K. Naidoo, K. M. L. Cramb, M. C. Caiazza, A. B. Malpartida, M. Lavelle, K. Savory, S. W. Humble, R. Patterson, J. B. Davis, N. Connor-Robson, B. J. Ryan, R. Wade-Martins, Mitochondrial

dysfunction and mitophagy defects in LRRK2-R1441C Parkinson's disease models. *Hum. Mol. Genet.* **32**, 2808–2821 (2023).
40. C. G. Weindel, E. L. Martinez, X. Zhao, C. J. Mabry, S. L. Bell, K. J. Vail, A. K. Coleman, J. J. VanPortfliet, B. Zhao, A. R. Wagner, S. Azam, H. M. Scott, P. Li, A. P. West, J. Karpac, K. L. Patrick, R. O. Watson, Mitochondrial ROS promotes susceptibility to infection via gasdermin D-mediated necroptosis. *Cell* **185**, 3214–3231.e23 (2022).
41. F. Di Domenico, R. Sultana, A. Ferree, K. Smith, E. Barone, M. Perluigi, R. Coccia, W. Pierce, J. Cai, C. Mancuso, R. Squillace, M. Wiengele, I. Dalle-Donne, B. Wolozin, D. A. Butterfield, Redox proteomics analyses of the influence of co-expression of wild-type or mutated LRRK2 and Tau on *C. elegans* protein expression and oxidative modification: Relevance to Parkinson disease. *Antioxid. Redox Signal.* **17**, 1490–1506 (2012).
42. S. A. Belambri, M. Hurtado-Nedelec, A. Senator, K. Makni-Maalej, M. Fay, M. A. Gougerot-Pocidalo, J. C. Marie, P. M. Dang, J. el-Benna, Phosphorylation of p47phox is required for receptor-mediated NADPH oxidase/NOX2 activation in Epstein-Barr virus-transformed human B lymphocytes. *Am. J. Blood Res.* **2**, 187–193 (2012).
43. F. Gao, D. Chen, Q. Hu, G. Wang, Rotenone directly induces BV2 cell activation via the p38 MAPK pathway. *PLOS ONE* **8**, e72046 (2013).
44. T. Eguchi, M. Sakurai, Y. Wang, C. Saito, G. Yoshii, T. Wileman, N. Mizushima, T. Kuwahara, T. Iwatsubo, The V-ATPase-ATG16L1 axis recruits LRRK2 to facilitate the lysosomal stress response. *J. Cell Biol.* **223**, e202302067 (2024).
45. R. Qi, E. Sammler, C. P. Gonzalez-Hunt, I. Barraza, N. Pena, J. P. Rouanet, Y. Naaldijk, S. Goodson, M. Fuzzati, F. Blandini, K. I. Erickson, A. M. Weinstein, M. W. Lutz, J. B. Kwok, G. M. Halliday, N. Dzamko, S. Padmanabhan, R. N. Alcalay, C. Waters, P. Hogarth, T. Simuni, D. Smith, C. Marras, F. Tonelli, D. R. Alessi, A. B. West, S. Shiva, S. Hilfiker, L. H. Sanders, A blood-based marker of mitochondrial DNA damage in Parkinson's disease. *Sci. Transl. Med.* **15**, eabo1557 (2023).
46. R. Di Maio, P. J. Barrett, E. K. Hoffman, C. W. Barrett, A. Zharikov, A. Borah, X. Hu, J. McCoy, C. T. Chu, E. A. Burton, T. G. Hastings, J. T. Greenamyre, α-Synuclein binds to TOM20 and inhibits mitochondrial protein import in Parkinson's disease. *Sci. Transl. Med.* **8**, 342ra378 (2016).
47. W. Y. Sun, V. A. Tyurin, K. Mikulska-Ruminska, I. H. Shrivastava, T. S. Anthonymuthu, Y. J. Zhai, M. H. Pan, H. B. Gong, D. H. Lu, J. Sun, W. J. Duan, S. Korolev, A. Y. Abramov, P. R. Angelova, I. Miller, O. Beharier, G. W. Mao, H. H. Dar, A. A. Kapralov, A. A. Amoscato, T. G. Hastings, T. J. Greenamyre, C. T. Chu, Y. Sadovsky, I. Bahar, H. Bayır, Y. Y. Tyurina, R.-R. He, V. E. Kagan, Phospholipase iPLA$_2\beta$ averts ferroptosis by eliminating a redox lipid death signal. *Nat. Chem. Biol.* **17**, 465–476 (2021).
48. Y. Y. Tyurina, A. M. Polimova, E. Maciel, V. A. Tyurin, V. I. Kapralova, D. E. Winnica, A. S. Vikulina, M. R. M. Domingues, J. McCoy, L. H. Sanders, H. Bayır, J. T. Greenamyre, V. E. Kagan, LC/MS analysis of cardiolipins in substantia nigra and plasma of rotenone-treated rats: Implication for mitochondrial dysfunction in Parkinson's disease. *Free Radic. Res.* **49**, 681–691 (2015).
49. J. R. Cannon, V. Tapias, H. M. Na, A. S. Honick, R. E. Drolet, J. T. Greenamyre, A highly reproducible rotenone model of Parkinson's disease. *Neurobiol. Dis.* **34**, 279–290 (2009).
50. N. Kumar, A. F. Theil, V. Roginskaya, Y. Ali, M. Calderon, S. C. Watkins, R. P. Barnes, P. L. Opresko, A. Pines, H. Lans, W. Vermeulen, B. van Houten, Global and transcription-coupled repair of 8-oxoG is initiated by nucleotide excision repair proteins. *Nat. Commun.* **13**, 974 (2022).

Acknowledgments: Figure S12 was made using BioRender (publication license no. TE25YQBTH5). **Funding:** This study was supported by NIH grant no. R56 NS131137-01 (J.T.G.), the Blechman Foundation for Parkinson's Research (J.T.G.), the friends and family of S. Logan (J.T.G.), the American Parkinson Disease Association Center for Advanced Research at the University of Pittsburgh (J.T.G.), the Michael J Fox Foundation Pritzker Prize (J.T.G.), and Commonwealth of Pennsylvania grant no. 601457 (J.T.G.). **Author contributions:** J.T.G. and M.T.K. conceived the study, managed the project, designed experiments, interpreted results, and wrote the paper, with assistance from all authors. M.T.K., R.D.M., B.R.D.M., P.J.P., S.A.P., W.D.S., T.G.H., and J.T.G. contributed to the design of in vitro and in vivo experiments. M.T.K., E.M.R., E.K.H., J.W., W.G.W., X.H., MF, C.L.C., A.S., and K.F. performed in vitro or in vivo experiments. M.T.K., J.W., W.G.W., and CLC performed the PL assay and immunoblot experiments. E.K.H. created CRISPR-Cas9 gene-edited HEK293 cell lines. **Competing interests:** M.T.K., S.A.P., W.D.S., and J.T.G. are co-inventors on a patent application entitled "Methods of Lowering LRRK2." W.D.S. and S.A.P. are full-time employees of Acurex Biosciences and also own stock in the company. E.M.R. is principal investigator and J.T.G. is co-investigator of a sponsored research agreement between Acurex Biosciences and the University of Pittsburgh. The other authors declare that they have no competing interests. **Data and materials availability:** All data associated with the paper are in the main text or the Supplementary Materials. CRISPR-Cas9 gene-edited HEK293 (G2019S, R1441G, and LRRK2$^{-/-}$) cell lines are available upon request to J.T.G. under a materials transfer agreement with the University of Pittsburgh. Patient-derived lymphoblastoid cell lines were obtained from Coriell Institute.

Submitted 13 October 2023
Resubmitted 30 April 2024
Accepted 12 September 2024
Published 2 October 2024
10.1126/scitranslmed.adl3438